

1 **The cellular architecture of microvessels, pericytes and neuronal cell types in organizing**
2 **regional brain energy homeostasis in mice**

3

4

5 Yuan-ting Wu^{1,*}, Hannah C. Bennett^{1,*}, Uree Chon¹, Daniel J. Vanselow², Qingguang Zhang³,
6 Rodrigo Muñoz-Castañeda⁴, Keith C. Cheng³, Pavel Osten⁴, Patrick J. Drew^{3,5}, Yongsoo Kim¹

7

8

9

10 1 Department of Neural and Behavioral Sciences, The Pennsylvania State University, Hershey,
11 PA, USA

12 2 Department of Pathology, The Pennsylvania State University, Hershey, PA, USA

13 3 Center for Neural Engineering, Department of Engineering Science and Mechanics, The
14 Pennsylvania State University, University Park, PA, USA.

15 4 Cold Spring Harbor Laboratory, Cold Spring Harbor, NY, USA

16 5 Biomedical Engineering, and Neurosurgery, The Pennsylvania State University, University
17 Park, PA, USA

18

19 *Co-First author

20

21

22

23

24 Corresponding author:

25 Yongsoo Kim

26 Email: yuk17@psu.edu

27

28

29

30

31

32

33 Keywords: Cerebral vasculature, microvessel, pericyte, brain mapping, hemodynamics,
34 parvalbumin, nNOS, vGlut1

35

36

37 **Abstract**

38

39 The cerebrovascular network and its mural cells must meet the dynamic energy demands of
40 different neuronal cell types across the brain, but their spatial relationship among these cells is
41 largely unknown. Here, we apply brain-wide mapping methods to create a comprehensive
42 cellular-resolution resource comprising the distribution of and quantitative relationship between
43 microvessels, pericytes, and glutamatergic and GABAergic neurons including neuronal nitric
44 oxide synthase-positive (nNOS+) neurons and their subtypes in mice. Leveraging these data, we
45 discovered region-specific signatures of vasculature and cell type compositions across cortical
46 and subcortical areas, including strikingly contrasting correlations between the density of
47 vasculature, pericytes, glutamatergic neurons and parvalbumin-positive interneurons versus
48 nNOS+ neurons in the isocortex. We also found surprisingly low vasculature and pericyte
49 density in the hippocampus, and distinctly high pericyte to vasculature ratio in the hypothalamus.
50 These findings suggest that vascular density and mural cell composition is finely tuned to
51 maintain regional energy homeostasis.

52

53

54

55

56

57

58

59

60

61 Introduction

62
63 The brain is the most energy-demanding organ per gram and is powered by an intricate web of
64 vascular and mural cells that dynamically supply blood and clear metabolic waste (Hartmann et
65 al., 2015; Sweeney et al., 2016; van Veluw et al., 2020; Vergara et al., 2019; Zhao et al., 2015).
66 Pericytes, a key mural cell type, wrap around microvessels and are proposed to regulate blood
67 flow and vascular permeability (Hall et al., 2014; Hartmann et al., 2021; Hill et al., 2015;
68 Howarth et al., 2021; Nikolakopoulou et al., 2019; Rungta et al., 2018; Sweeney et al., 2016).
69 Moreover, neuronal activity is known to regulate vascular diameter directly or indirectly (via
70 astrocytes), which is referred to as a neurovascular coupling (Attwell et al., 2010; Kaplan et al.,
71 2020). Neurons, unlike muscle, strictly rely on aerobic metabolism, thus neuronal functions
72 critically depend on efficient vasculature support (Hall et al., 2012; Vergara et al., 2019). Not
73 surprisingly, impairment of the cerebrovasculature, pericytes, and neurovascular coupling has
74 been widely implicated in many neurological disorders such as stroke and neurodegenerative
75 disorders (Lecrux and Hamel, 2011; Zhao et al., 2015). Yet, despite its significance, we have
76 limited knowledge on the cellular architecture of vasculature and pericytes, especially with
77 respect to their quantitative relationship with neuronal cell types across the whole brain. This
78 relationship is likely of critical importance for the heterogeneous coupling of neural activity to
79 blood flow described across different brain regions (Boido et al., 2019; Devonshire et al., 2012;
80 Huo et al., 2014; Shih et al., 2009; Zhang et al., 2019a).

81 The generation of action potentials and synaptic transmission are energetically demanding
82 (Howarth et al., 2012) and accordingly energy consumption is proposed to be linearly correlated
83 with the number of neurons across different animal species including humans (Herculano-
84 Houzel, 2011). However, neurons comprise highly distinct subtypes with different
85 morphological, electrophysiological, and molecular characteristics (Kepecs and Fishell, 2014;
86 Tasic et al., 2018). For example, the major classes of GABAergic neurons in the cortex include
87 parvalbumin (PV), somatostatin (SST), and vasoactive intestinal peptide (VIP) expressing
88 neurons, each of which make distinct synaptic connections with pyramidal neurons and each
89 other (Kepecs and Fishell, 2014). Moreover, these neuronal cell types are expressed at different
90 densities across cortical areas: PV interneurons have high density in sensory cortices and low
91 density in association cortices, while SST neurons showed the opposite density pattern in mice
92 (Kim et al., 2017). Different neuronal subtypes also have differential energy demands. For
93 instance, the fast spiking PV neurons are among the highest energy demanding neuronal types
94 (Inan et al., 2016). On the other hand, another neuronal type – the neuronal nitric oxide synthase
95 (nNOS) expressing neurons – can actively regulate blood supply by causing vasodilation
96 (Echagarruga et al., 2020; Krawchuk et al., 2020; Lee et al., 2020). Taken together, these data
97 suggest that determining specific spatial relationships between neuronal cell types and the
98 vascular network is critically important for understanding the demand for and the mechanism of
99 distinct blood flow regulation across different brain regions.

100
101 It has been technically challenging to comprehensively examine mammalian cerebrovasculature
102 because of its fine and complex branching across the entire brain, with the diameter of small
103 capillaries being only $\sim 5\mu\text{m}$. However, recent progress in meso-scale mapping methods began
104 elucidating the structural organization of the cerebrovasculature and its regional heterogeneity
105 across the mouse brain at unprecedented detail (Ji et al., 2021; Kirst et al., 2020; Todorov et al.,
106 2020; Xiong et al., 2017). However, while these studies provide a detailed description of the

107 general organization of mouse brain cerebrovasculature, the question of how cerebrovasculature
108 and its mural cells are structurally organized to support different neuronal cell types across the
109 whole brain remains largely unanswered. To address the relationship between cerebrovasculature
110 and mural and neuronal cell types, we have devised a serial two-photon tomography (STPT)-
111 based imaging approach with newly developed analytical tools to derive the first cellular
112 architecture atlas containing cerebrovasculature, capillary pericytes, and several major neuronal
113 cell types, including PV interneurons and vasomotor nNOS neurons in the adult mouse brain.

114
115 Leveraging this data resource, we asked the following questions about the quantitative
116 relationship of vasculature and associated cell types in different brain regions, with emphasis on
117 the isocortex due to the well-established functional roles of cortical neuronal subtypes. (1) Are
118 densities of microvessels and pericytes uniform across the entire cortex or are there distinct
119 spatial patterns that may be linked to the densities of neuronal cell types, such as the energy
120 demanding PV neurons and vasomotor nNOS neurons? And (2) does blood perfusion via
121 microvessels occur evenly in 3D across the cortex, or are there directional preferences based on
122 cortical layers or different cortical areas? Answering these two questions will help to elucidate
123 local cerebrovascular organization principles and shed light on how distinct cortical domains
124 maintain balance between energy demands and supplies. Lastly, we also asked whether (3) there
125 are areas with distinct vascularization and pericyte coverage that may predispose certain brain
126 areas to pathological conditions. For instance, impairment of the hippocampus and association
127 cortical areas are frequently associated with neurodegenerative disorders such as Alzheimer's
128 disease (Ballinger et al., 2016; Sweeney et al., 2018). Comparing vascular networks in these
129 regions to other areas may help to explain brain regional vulnerabilities.

130
131

132 **Results**

133

134 **Comprehensive vascular mapping in the intact mouse brain**

135 Our first goal is to examine the spatial arrangement of the cerebrovasculature in an intact whole
136 mouse brain to understand the anatomical basis of the vascular network. We filled microvessels
137 from 2-month-old C57BL/6 mice with a cardiac perfusion of FITC-conjugated albumin gel
138 (Figure 1A)(Blinder et al., 2013; Tsai et al., 2009) and used STPT imaging in combination with
139 two-photon optical scans and serial sectioning to image the whole mouse brain at $1 \times 1 \times 5 \mu\text{m}$
140 (x, y, z ; media-lateral, dorsal-ventral, rostral-caudal) (Figure 1B). Since the vascular tracing
141 requires precise stitching across X-Y tiles throughout z stacks, we developed a new stitching
142 algorithm to correct optical aberrations, bleaching in overlapped tile areas, and z stack
143 alignments (Figure 1C-D; Figure S1). To detect and analyze cerebrovascular arrangement, we
144 developed a computational pipeline that binarizes and traces the original image of the FITC-
145 filled vasculature, as well as quantifies the diameter of each vessel and its branching points
146 across the whole brain (Figure 1E-G; See Methods for more details). Individual brains were then
147 registered to the Allen Common Coordinate Framework (CCF) to quantify signals across
148 different anatomical areas (Wang et al., 2020) (Figure 1H-N; Table S1; MovieS1). Although we
149 observed near-complete vasculature labeling with our FITC-based filling approach, we
150 implemented an additional quality control step to reject data from areas with potentially
151 incomplete labeling or imaging artifacts (Figure S1). Moreover, we confirmed that our approach
152 closely reflects vasculature *in vivo* by directly comparing STPT results with *in vivo* two-photon
153 measurements of the same vasculature in same mice (Figure S2).

154 Initial analysis of this data revealed that for vascular density, there is up to a three-fold
155 difference between highly (e.g., cerebellar nuclei) and sparsely vascularized regions (e.g., medial
156 amygdala)(Figure 1K-N). For example, the cerebellum, midbrain, and thalamic areas have high
157 vascular density while the cortex, hippocampus, amygdala, and hypothalamic regions show
158 overall low vascular density (Figure 1K-L). These results are consistent with recent studies to
159 quantify vascular densities in the mouse brain, further confirming that there are vascular density
160 differences across the brain based on regionally heterogenous metabolic needs (Ji et al., 2021;
161 Kirst et al., 2020).

162 Since vascular branching represents the degree of connectivity in the vasculature, we ask
163 how vascular branching density is quantitatively related to vascular length density across brain
164 regions (Figure 1M). If the vascular density increases while maintaining their connectivity, we
165 can expect that branching density will proportionally increase to the power of 1.5. Our result
166 shows that the branching density increases to the power of 1.183, indicating that vascular
167 branches have lower connectivity as vascular density increases (Figure 1M). In contrast, vascular
168 radii do not show significant correlation with vascular density (Figure 1N).

169

170 **Vasculature across the isocortex is not uniform**

171 The mouse isocortex, particularly the primary somatosensory cortex, has been a major area of
172 focus for *in vivo* studies examining the cellular mechanisms of neurovascular coupling
173 (Echagarruga et al., 2020; Hill et al., 2015; Krawchuk et al., 2020; Vazquez et al., 2018). Yet, it
174 is not known whether the vasculature is anatomically organized in a similar way across the entire
175 cortex or whether different cortical areas may have unique vascular organization signatures and
176 consequently different neurovascular coupling (Huo et al., 2014; Zhang et al., 2019a).

177 We found highly regionally heterogeneous vascular distribution in the isocortex, with
178 unique patterns for distinct functional cortical areas (Figure 2). Sensory motor areas such as
179 somatosensory (SS) and auditory cortices (AUD) showed overall high vascular density,
180 branching density, and radii while medial prefrontal areas including prelimbic (PL), medial
181 orbital (ORBm), and infralimbic (ILA) were low on all three measurements (Figure 2A-B). In
182 contrast, many lateral association areas including the posterior agranular insular (AIP), ECT, and
183 PERI showed high vascular diameter with relatively lower vascular density (Figure 2A-B).
184 Noticeably, the retrosplenial cortex (RSP), linked with spatial navigation and memory processing
185 (Mitchell et al., 2018), has low vascular diameter despite high vascular density (Figure 2A-B).
186 To examine the spatial distribution intuitively while maintaining high resolution information, we
187 devised an isocortical flatmap based on Laplace's equation (Figure 2C-F; see Methods for more
188 details). When averaged vessel length density is plotted in the cortical flatmap, it is clear that
189 densely vascularized areas are tightly aligned with anatomical borders of the SS, AUD, visual
190 (VIS), and RSP cortices (Figure 2G, arrowheads). Cortical layer-specific maximum projection of
191 the length density shows that sharp boundaries between cortical areas are strongly driven by the
192 layer 2/3/4 vascular distribution (Figure 2H). Interestingly, one measure of the cortical
193 vasculature that did not show strong regional differences is the vessel radius, which is relatively
194 similar across cortical areas with the exception of the RSP that comprises vessels with low
195 vascular diameter (Figure 2G).

196 Taken together, these data provide strong evidence that cortical vascularization is not
197 uniform but is distinctly organized in functionally different cortical areas.

198
199

200 **Quantification of permeability reveals spatial heterogeneity of the vasculature network**

201 Since microvessels provide a large surface area to exchange oxygen and glucose, we examined
202 the link between microvessel structure and its influence on blood perfusion in the brain by
203 applying a mathematical approach to infer permeability to blood flow and directionality of the
204 microvascular network based on our vascular measurements (Figure 3A; Movie S2; Table S2).
205 To limit our simulation to small vessels, we removed large vessels with radius $> 4 \mu\text{m}$. The
206 permeability was calculated through solving the Hagen–Poiseuille equation system of the entire
207 network in the control volume (Figure 3A), taking into account vascular density, connectivity,
208 and network topology (e.g., tortuosity). For example, a network twice as dense with identical
209 topology will have doubled permeability (Figure 3B; length density), while doubling the vascular
210 radius of an identical network gives a sixteen-fold increase in permeability (Figure 3B; vessel
211 radius). With respect to vascular topology, a bias in the orientation of the vasculature will lead to
212 a higher permeability tensor in parallel to the vessel, but a lower permeability in orthogonal
213 directions (Figure 3B; directionality), and a highly twisted network can significantly reduce the
214 permeability (Figure 3B; tortuosity). After probing the permeability of a given microvessel in all
215 directions, we spherically integrated the permeability tensor, yielding a scalar as final
216 permeability output (Figure 3B) representing how well blood can pass through microvessels at a
217 given input from the arteries.

218 We present two examples from the isocortex, one is the primary somatosensory cortex
219 barrel field (SSp-bfd) with relatively higher permeability, and the other one is the ORBm in the
220 medial prefrontal cortex with poor permeability (Figure 3C). Higher permeability of the SSp-bfd
221 occurs due to the high density of vasculature that is arranged in all directions despite higher
222 vascular tortuosity (Figure 3C, left side). In contrast, the lower permeability of the ORBm is

223 largely driven by low vascular density despite its relatively lower tortuosity (Figure 3C, right
224 side). Across isocortical areas, sensory-motor and RSP areas have overall higher permeability
225 compared to medial prefrontal and lateral association areas (Figure 3D; Table S2).

226 Since the geometry of microvascular networks can influence directionality of blood flow,
227 we examined the microvessel anisotropy using the permeability tensor in the isocortex (Figure
228 3E-I). We used three axes according to the cortical column direction: penetrating (P) axis along
229 the cortical column, anterior-posterior (AP), and medial-lateral (ML) (Figure 3G). Our analysis
230 showed that microvessels oriented in the P-axis dominated in the anterior (e.g., motor areas) and
231 posterior cortical areas (e.g., visual area) while mid-cortical areas (e.g., somatosensory area)
232 showed vasculature orientation in the P and AP axes dominating the superficial layer and the
233 deep layers, respectively (Figure 3E-I). For instance, the secondary motor cortex (MOs) shows
234 dominant P-axis vasculature (magenta) while the SS_{Sp}-bfd shows clear switch to AP axis (cyan)
235 vasculature preferentially between layers 4 – 6 (Figure 3E-F). Collectively, our data demonstrate
236 that the isocortex contains different cortical domains with area and cortical layer specific
237 microvascular perfusion patterns.

238 When we applied the permeability measurement across the whole brain, we found that
239 the thalamic area (e.g., VENT), cortical subplate areas (e.g., BLA), selected midbrain areas
240 including the inferior colliculus (IC) show higher permeability (Figure 3J; Figure S3; Table S2;
241 Movie S2). In contrast, many hippocampus areas including the dentate gyrus (DG) and the
242 subiculum (SUB) showed low permeability (Figure 3J; Figure S3; Table S2). This baseline
243 difference of microvascular permeability can help to explain regional vulnerabilities of
244 hippocampal areas in association with many neurodegenerative disorders (Ballinger et al., 2016;
245 Sweeney et al., 2018).

247 **Pericyte density mapping reveals differential pericyte coverage between cortical and** 248 **subcortical areas**

249 Pericytes encapsulate the microvasculature and are thought to actively regulate microvascular
250 diameter and permeability (Attwell et al., 2016; Bennett and Kim, 2021; Hartmann et al., 2021;
251 Nelson et al., 2020; Nikolakopoulou et al., 2019). Here, we ask whether pericyte density in
252 different brain areas parallels that of cortical vasculature and whether the ratios of pericyte to
253 vascular density may differ by brain area. To map pericyte distribution, we crossed PDGFR β -Cre
254 mice with Ai14 reporter mice (PDGFR β -Cre: Ai14 mice) to fluorescently label vascular mural
255 cells (Cuttler et al., 2011; Hartmann et al., 2015) and imaged their whole brain distribution by
256 STPT (Figure 4A-B). To conduct whole brain quantification of this cell population, we
257 developed a new machine learning algorithm to specifically count capillary pericytes from
258 fluorescently-labeled cells in PDGFR β -Cre: Ai14 mice (Figure 4C; Figure S4; Table S3; Movie
259 S3; see the methods section for more details). Furthermore, we used our previously established
260 qBrain mapping pipeline to map the signals onto the adult CCF (Kim et al., 2017; Wang et al.,
261 2020) and quantify the 3D density of the pericyte distribution across the whole brain (Figure 4C-
262 H; Table S4; see the methods section for more details).

263 When we examined the regions of the isocortex, we found that cortical pericyte density
264 showed a similar distribution pattern to the vascular density (Figure 4C-D; Tables S4). While the
265 sensory motor areas, including the somatosensory and auditory regions as well as the RSP,
266 contain a higher density of pericytes, the medial prefrontal and lateral association cortices show
267 lower pericyte density (Figure 4C-D; Table S4). Moreover, when comparing cortical layers,
268 layers 4 and 5 contain the highest density of pericytes across the whole isocortex, while layer 1

269 contains the lowest pericyte density (Figure 4D; Table S4). This is particularly apparent in
270 regions of high pericyte density, such as the somatosensory and auditory cortices. Overall,
271 cortical pericyte density shows strong positive correlation with vascular length density (Figure
272 4E).

273 For the rest of the brain, we found pericyte density varied by a factor of two across
274 different brain areas and showed significantly positive correlation with vascular density across
275 the brain (Figure 4F-H; Table S4). Noticeably, cortical sensory circuit pathways including
276 sensory thalamic nuclei (e.g., ventral group of dorsal thalamus; VENT, Dorsal lateral geniculate
277 nucleus; LGd) are among the high-density groups while memory circuit pathways including the
278 DG of the hippocampus and mammillary body (MBO) are among the low-density group (Figure
279 4F-H; Table S4). Furthermore, many hypothalamic areas (e.g., anterior hypothalamic nucleus;
280 AHN) have relatively high pericyte density despite low vascular density (Figure 4G).
281 In summary, our pericyte mapping results reveal positive correlations with microvascular density
282 but with extensive regional heterogeneity across the whole brain.

283

284 **Cell type mapping with genetic intersection approach reveals regionally distinct nNOS** 285 **subtypes expression**

286 Next, we examined the relationship between the cerebrovascular network with pericytes and the
287 distribution of nNOS-expressing neurons that are known to control neurovascular coupling in the
288 brain (Echagarruga et al., 2020; Krawchuk et al., 2020; Lee et al., 2020). We employed a genetic
289 labeling method using nNOS-CreER mice with postnatal tamoxifen induction (Figure
290 5A)(Taniguchi et al., 2011). Since nNOS neurons also contain different subtypes co-expressing
291 SST, NPY, PV, or VIP, which are linked with distinct functions including regulating vascular
292 diameter (Perrenoud et al., 2012; Tricoire and Vitalis, 2012; Williams et al., 2017), we utilized
293 genetic intersection methods using Cre and Flp dependent reporter mice (Ai65) crossed with
294 nNOS-CreER and one of the subtype markers (NPY-, SST-, PV-, or VIP-Flp), in combination
295 with tamoxifen induction (Figure 5A)(He et al., 2016). Then, we used the qBrain mapping
296 method with new nNOS detection algorithms to examine reporter gene expression from these
297 different mouse lines (Figure 5B-E; Figure 3S; Movie S4; Table S5).

298 Our results indicate that the total nNOS neuronal density is highest in the accessory
299 olfactory bulb, the striatum-like amygdala (e.g., the medial amygdala), the hypothalamus, and
300 the cerebellum (Figure 5F-H). In contrast, the isocortex, the hippocampus, and the thalamus
301 showed relatively lower overall nNOS neuronal density (Figure 5F-H). The nNOS/NPY neurons
302 represent the majority of nNOS subtypes in cerebral cortical and cerebral nuclei areas, including
303 hippocampal areas (Figure 5F-H). The nNOS/SST subtype showed similar density compared to
304 the nNOS/NPY subtype overall, but with lower density in hippocampal regions (Figure 5F-H).
305 The nNOS/PV subtype showed overall low density across the whole brain, except for very high
306 density in the cerebellum (Figure 5F-H). Lastly, the nNOS/VIP subtype had the lowest density
307 compared to the other nNOS⁺ subtypes, except in a few areas, such as the subiculum of the
308 hippocampus, where the density was modest (Figure 5F-H). Noticeably, many amygdala and
309 hypothalamic areas as well as the accessory olfactory bulb showed high nNOS density that was
310 not reflected in the nNOS interneuron subtype populations, suggesting that nNOS neurons in
311 these areas may represent different nNOS subtypes (Chachlaki et al., 2017).

312

313 **Cortical nNOS neurons are negatively correlated with vascular and pericyte densities**

314 Since the vasomotor function of cortical nNOS neurons is well-established (Echagarruga et al.,
315 2020; Lourenço et al., 2017; Perrenoud et al., 2012), we examined whether the density
316 distribution of nNOS neurons in the isocortex is significantly correlated with the density of
317 cerebrovasculature and pericytes. Overall, we observed up to two-fold differences in nNOS
318 neuronal density across isocortical brain regions (Figure 5I-K; Table S5). Surprisingly, nNOS
319 neurons showed higher expression in the medial and lateral association cortices (e.g., the
320 agranular insular cortex), while sensory-motor areas as well as the RSP showed lower density,
321 which is the opposite of the vascular density pattern (Figure 5I,K). The highest density of nNOS
322 neurons is found in layer 6 in all cortical areas (Figure 5I). For nNOS subtypes, nNOS/NPY and
323 nNOS/SST subtypes showed similar density patterns with the total nNOS neurons (Figure 5J-K).
324 In contrast, nNOS/PV and nNOS/VIP subtypes, despite much lower density, showed relatively
325 higher expression in the RSP and the lateral cortex, respectively (Figure 5J-K). When we
326 performed correlation analysis for the relationship between nNOS density and vascular density
327 across different areas, we found a significant negative correlation in the isocortex (Figure 5L).
328 All subtypes except nNOS/PV showed a similar negative correlation with vascular density
329 (Figure 5M). Similarly, nNOS neurons, including nNOS/NPY and nNOS/VIP subtypes, showed
330 significant negative correlation with pericyte density (Figure 5M). In contrast, nNOS neurons
331 and all of their subtypes did not show any correlation with average vasculature radius (Figure
332 5M). This data suggests that cortical nNOS neurons have overall stronger vasomotor regulation
333 in high association cortices than in sensory cortices.

334 335 **Cortical PV interneurons and glutamatergic neurons show positive correlation with the** 336 **vascular network**

337 Glutamatergic and GABAergic neuronal cell types have different energy consumption and
338 metabolic costs (Buzsáki et al., 2007). Here, we examined whether specific neuronal subtypes
339 show any significant correlation with vascular and pericyte distribution in the isocortex (Figure
340 6; Table 1; Table S6). We used pan-glutamatergic (vGlut1) and pan-GABAergic (Gad2) Cre
341 driver lines crossed with conditional nuclear tdTomato reporter mice (Ai75) and used the qBrain
342 mapping method to quantify each cell type signal and map the distribution onto our isocortical
343 flatmap (Figure 6; Movie S5). For non-overlapping GABAergic interneuron subtypes PV, SST,
344 and VIP interneurons, we used our previously mapped data based on the cell type specific Cre
345 drivers crossed with conditional nuclear GFP reporter mice (Kim et al., 2017)(Figure 6A-C).
346 Density plotting using our isocortical flatmap demonstrates the different neuronal cell type
347 distributions and localizations across the isocortex, and shows a clear pattern when compared to
348 the vessel length and pericyte densities (Figure 6C). Among GABAergic cell types, PV
349 interneurons show a strikingly significant positive correlation with the vascular length density
350 (Figure 6C-E). All sensory cortical areas, including the primary somatosensory cortex, showed
351 high PV interneuron and vascular density (Figure 6B-E). In contrast, the other interneuron
352 subtypes (SST and VIP) and pan-GABA (Gad2) did not show a significant correlation with
353 vascular density (Figure 6C-E). Lastly, pan-glutamatergic neurons (vGlut1) showed significant
354 positive correlation with vascular density (Figure 6C,E). As expected, the pericyte distribution
355 mirrored the same correlation patterns as the vessel length density with all of the neuronal
356 subtypes studied (Figure 6E). Importantly, cortical PV neurons are involved in the generation of
357 gamma-band oscillations (Cardin et al., 2009; Sohal et al., 2009), which are linked with
358 increased vasodilation and blood flow in the brain (Drew et al., 2020). Thus, our results suggest

359 that neurovascular and pericyte density are proportionally distributed to the PV neurons in order
360 to support local neural activity in sensory cortices.

361

362

363 **Web visualization**

364 Ease of access and intuitive visualization is a key when examining large scale imaging datasets.

365 Toward these goals, we created a web-based resource (<https://kimlab.io/brain-map/nvu/>) that
366 displays navigable z-stacks of full-resolution images for our STPT datasets including FITC filled
367 vasculature, PDGFR β -Cre: Ai14 for pericytes, nNOS-Cre: Ai14 for total nNOS neurons, and
368 nNOS-Cre: Ai65:(NPY, SST, PV, or VIP-Flp) for nNOS subtypes. This web-based resource also
369 provides interactive 3D visualizations, allowing users to navigate our quantitative vascular and
370 cell type measurements registered in the Allen CCF.

371

372 **Discussion**

373 The structural organization of regional vascular networks is crucial to understand their function
374 as well as susceptibility to pathology. Here we present cellular resolution maps of cerebral
375 vasculature, pericytes, and neuronal subtypes in the mouse brain. Our cerebrovascular map, in
376 combination with fluid dynamic simulations, reveals differential coverages of microvessels and
377 pericytes as well as their relationships with neuronal cell types, highlighting heterogenous blood
378 perfusion and potential differences in regulation across different brain regions as exemplified in
379 Figure 7. Most notably, we observed strikingly strong correlations between vascular density and
380 parvalbumin interneuron and vasomotor nNOS neuron density in the isocortex, suggesting that
381 regional differences in neuronal cell type composition linked with different energy demands are
382 met by region-specific patterns of cortical vascularization. In combination with web
383 visualization, our maps serve as a comprehensive resource to examine microvasculature and
384 associated cell types.

385

386 **Cortical neuronal cell types and the vascular network**

387 A prevailing theory of cortical organization is that the cortex is composed of repeating cortical
388 columns with a common microcircuit motif (Douglas and Martin, 2004). For example, excitatory
389 and inhibitory neuronal subtypes make stereotypic local connection patterns, called canonical
390 cortical circuits, that are similarly observed across cortical areas (Packer and Yuste, 2011; Pi et
391 al., 2013). However, this view has been challenged by recent data that different cortical domains
392 show distinct cell type compositions and hemodynamic responses (Kim et al., 2017; Zhang et al.,
393 2019a). Results from the current study, as summarized in Figure 7 and Table 1, provide further
394 evidence that vascular networks, including pericytes and vasomotor neurons, are organized
395 differently to meet energy demand from sensory and association cortices (Howarth et al., 2012;
396 Vergara et al., 2019).

397 Sensory signals require precise temporal and spatial information processing in sensory
398 cortices such as the somatosensory cortex barrel field representing whisker-evoked stimuli in
399 rodents. In contrast, association cortices integrate information from broader areas with slower
400 temporal kinetics. We previously identified a higher density of PV neurons in sensory cortices
401 compared to association cortices (Kim et al., 2017). Cortical PV neurons are fast spiking
402 interneurons that participate in generating gamma oscillations and are one of the most energy
403 demanding neurons (Cardin et al., 2009; Hu and Jonas, 2014; Inan et al., 2016; Kann, 2016).
404 Thus, our current results suggest that a high density of microvessels and capillary pericytes in the
405 sensory cortices provide an efficient energy support system for PV dominated local circuits to
406 accommodate high energy consumption and handle high speed sensory processing. In contrast,
407 association cortices contain relatively high densities of nNOS neurons despite low vascular,
408 pericyte, and PV densities. Although nNOS interneurons represent only about 2% of cortical
409 neurons, activation of nNOS neurons robustly dilates cerebral arterioles to generate increases in
410 cerebral blood flow (Echagarruga et al., 2020; Hosford and Gourine, 2019; Krawchuk et al.,
411 2020; Lee et al., 2020). Moreover, type I nNOS neurons co-expressing NPY and SST in the deep
412 cortical layer are a rare cortical GABAergic type with long-range projection to other cortical
413 areas, which can help to synchronize activities of target areas (Melzer and Monyer, 2020;
414 Tomioka and Rockland, 2007; Tomioka et al., 2005). Thus, the relatively higher density of
415 nNOS/SST neurons in association areas suggests that this cell type can exert more powerful
416 vasodilation in larger areas to compensate for a lower vascular density in these high cognitive
417 areas, while also orchestrating vasodilation in other cortical areas.

418

419 **Microvascular map to understand regional blood flow**

420 We used serial two-photon tomography to visualize the whole cerebrovasculature at single
421 capillary resolution from intact mouse brains that closely represents physiological conditions,
422 confirmed by *in vivo* two-photon microscopy. Although recent approaches using light sheet
423 microscopy to examine fine cerebrovascular structure provide advantages in rapid data
424 acquisition as well as 3D immunolabeling to mark different vascular compartments (Kirst et al.,
425 2020; Todorov et al., 2020), the required tissue clearing methods can introduce microscopic
426 volume distortions, which can lead to inconsistent measurements (Ji et al., 2021). Indeed, our
427 vascular measurements (e.g., length density) are consistent with other recent data that utilized
428 serial two-photon microscopy (Ji et al., 2021).

429 Our detailed geometric analysis of microvessels enables us to quantify vascular
430 permeability across different brain areas as a first step to building a more comprehensive model
431 of cerebral perfusion. Our permeability measurements represent potential blood flow efficiency
432 based on structural arrangements of microvessels upon a given input. The frontal cortical and
433 hippocampal areas are highly vulnerable in normal aging and neurodegenerative disorders such
434 as Alzheimer's disease (Sengillo et al., 2013; Zhang et al., 2019b). Our results suggest that these
435 areas have overall low microvessel permeability with low vascular densities, even at the baseline
436 condition, providing further evidence of the regional vulnerability to microvascular insults. Our
437 results also highlight area and layer specific vascular anisotropy in the isocortex, which is
438 consistent with recent studies (Ji et al., 2021; Kirst et al., 2020). However, the functional
439 significance of this vascular anisotropy remains unclear. Future works including computational
440 modeling considering additional information (e.g., blood pressure and viscosity) can help to gain
441 a more complete understanding of brain blood perfusion (Balogh and Bagchi, 2019; Blinder et
442 al., 2010).

443

444 **Brain-wide pericyte map**

445 Pericytes actively regulate the diameter and permeability of microvessels (Hartmann et al., 2021;
446 Nikolakopoulou et al., 2019). For example, optogenetic stimulation of capillary pericytes in the
447 cortex induces vasoconstriction, reducing red blood cell flux up to 50% (Hartmann et al., 2021;
448 Nelson et al., 2020). Our results complement this work by providing pericyte density across the
449 brain. We observed a strong positive relationship between pericyte and vascular density in the
450 cortex, suggesting that pericyte coverage per microvessel remains similar across different
451 cortical areas in the normal adult mouse brain. Moreover, subcortical mapping results indicate
452 that thalamic areas have overall higher pericyte density. Interestingly, thalamic pericytes showed
453 resistance to disrupted PDGFR β signaling, while cortical and striatal pericytes were vulnerable
454 (Nikolakopoulou et al., 2017). The combination of high density and cellular resilience may
455 confer extra protection to maintain vascular integrity in the thalamus. Conversely, relatively low
456 pericyte density in the hippocampal areas and association cortices can make these areas more
457 vulnerable to pathological conditions (Montagne et al., 2015; Sengillo et al., 2013; Zhao et al.,
458 2015).

459

460 In summary, our quantitative information on cerebrovasculature and associated cell types can
461 help to gain a cellular architectural basis of how energy demand and supply maintain balance in a
462 normal brain and how this homeostatic mechanism changes under pathological conditions in the
463 future.

464 **Material and Methods**

465

466 **Animals**

467 Animal experiments were approved by the Institutional Animal Care and Use Committee at Penn
468 State University and Cold Spring Harbor Laboratory. For all genotypes in this study, both adult
469 male and female mice were used. Adult 2-month-old C57BL/6 mice were bred from C57BL/6
470 mice directly obtained from the Jackson Laboratory and used for vascular tracing experiments
471 with FITC filling (N=4). For pericyte specific experiments, male PDGFR β -Cre mice (Cuttler et
472 al., 2011) were crossed with female Ai14 mice (Jax: Stock No: 007914) as previously described
473 (Hartmann et al., 2015). These PDGFR β -Cre: Ai14 mice exhibit PDGFR β -driven tdTomato
474 expression in two distinct vascular cell types, pericytes and vascular smooth muscle cells
475 (vSMCs). For isocortical cell types, vGlut1-Cre (Jax: 023527) and Gad2-Cre (Jax: 010802) mice
476 were crossed with Ai75 reporter mice (Jax: 025106). nNOS-CreER mice were used to label
477 nNOS neurons (Jax: Stock No: 014541)(Taniguchi et al., 2011). After nNOS-CreER mice were
478 crossed with Ai14 mice, the nNOS-CreER: Ai14 offspring were administered with an
479 intraperitoneal (i.p.) tamoxifen (Sigma, cat.no. T5648-1G) injection (100mg/kg) at P16.
480 Similarly, for nNOS-subtypes, nNOS-CreER mice were initially crossed with Ai65 mice (Jax;
481 Stock No: 021875), which were further crossed with PV-flp (Jax Stock No: 022730), SST-flp
482 (Jax Stock No: 028579), NPY-flp (Jax Stock No: 030211), or VIP-flp (Jax Stock No: 028578)
483 mouse lines, to generate triple transgenic mice which allowed for tdTomato fluorescent labeling
484 of nNOS expression within these interneuron populations. To allow for postnatal specific
485 expression of tdTomato in nNOS⁺ subtype populations, tamoxifen injections dosed at 75mg/kg
486 were given at P10, P12, and P14 timepoints. We used 10 animals for each PDGFR β : Ai14,
487 nNOS: Ai14, nNOS: VIP: Ai65, 9 animals for nNOS: NPY: Ai65 and nNOS: PV: Ai65, 8 animals
488 for nNOS: SST: Ai65 from both males and females as well as 7 animals (all males) for
489 vGlut1: Ai75, and 9 animals (all males) for Gad2: Ai75. We used tail genomic DNA with PCR for
490 genotyping. Brain samples were collected at 2 months old age for all mouse lines.

491

492 **Perfusion and tissue processing for STPT imaging**

493 Animals were deeply anesthetized with a ketamine-xylazine mixture (100 mg/kg ketamine, 10
494 mg/kg xylazine, i.p. injection) for both regular perfusion and vascular labeling. Transcardiac
495 perfusion with a peristaltic pump (Ismatec, cat.no.: EW-78018-02) was used with 1X PBS
496 followed by 4% paraformaldehyde, both injected through a small incision in the left ventricle, in
497 order to wash out blood and allow for tissue fixation, respectively. Brains were dissected
498 carefully in order to preserve all structures. For vessel labeling, transcardiac perfusion with a
499 peristaltic pump (Welch, Model 3100) was used with 1X PBS followed by 4% paraformaldehyde
500 at 0.3 ml/min, in order to wash out blood and for tissue fixation, respectively. To ensure that the
501 large surface vessels would remain filled with the gel perfusate, the body of the mouse was tilted
502 by 30° before gel perfusion (with the head tilted down), as previously described (Tsai et al.,
503 2009). Following the fixative perfusion, the mouse was perfused at 0.6 ml/min with 5 ml of a
504 0.1% (w/v) fluorescein isothiocyanate (FITC) conjugated albumin (Sigma-Aldrich, cat.no.:
505 A9771-1G) in a 2% (w/v) solution of porcine skin gelatin (Sigma-Aldrich, cat.no: G1890-500G)
506 in 1X PBS. Immediately after perfusion, the heart, ascending and descending aorta as well as the
507 superior vena cava, were all clamped with a hemostat (while the butterfly needle was
508 simultaneously removed from the left ventricle). This served to prevent any pressure changes in
509 or gel leakage from the brain vasculature. Next, the entire mouse body was submerged in an ice

510 bath to rapidly solidify the gel in the vessels. Then, the head was fixed in 4% PFA for one week,
511 followed by careful dissection of the brain to avoid damages to pial vessels. After fixation and
512 dissection, the brain was placed in 0.05M PB until imaging. Any animals that had poor perfusion
513 and/or possible air bubbles interfering with the gel perfusion were excluded from imaging and
514 any further analysis.

515

516 **Serial two photon tomography (STPT) imaging.**

517 Prior to imaging, the brain sample was embedded in oxidized agarose and cross-linked in 0.05M
518 sodium borohydrate at 4C for at least 2 days ahead of imaging (Kim et al., 2017; Newmaster et
519 al., 2019). This procedure allows for seamless cutting at 50 μ m thick sections, while also
520 preventing any tearing of the brain surface. The embedded brain sample was then glued to the
521 sample holder and fully submerged in 0.05M PB in an imaging chamber. For STPT imaging
522 (TissueCyte), we used 910nm excitation using a femtosecond laser (Coherent Ultra II) for all
523 samples. Signals in the green and red spectrum were simultaneously collected using a 560 nm
524 dichroic mirror (Chroma). For pericyte and neuronal subtypes, STPT imaging was conducted
525 with 1x1 μ m (x,y) resolution in every 50 μ m (z), with the imaging plane set at 40 μ m deep from
526 the surface, as previously described (Kim et al., 2017; Newmaster et al., 2019). For vascular
527 imaging, optical imaging (5 μ m z step, 10 steps to cover 50 μ m in z) was added in the imaging,
528 producing 1x1x5 μ m (x,y,z) resolution beginning at 20 μ m deep from the surface. Due to length
529 of imaging time required for vascular imaging, each brain sample was imaged through multiple
530 imaging runs to adjust the imaging window size in order to reduce overall imaging time.

531

532 **Computational: STPT Image reconstruction**

533 To measure and fix an optical aberration from an objective lens (Figure S1), we imaged a 25 μ m
534 EM-grid (SPI supplies, cat.no.: 2145C) to represent the ground truth spatial data (Han et al.,
535 2018). We annotated all cross points of the grid and computed the B-spline transformation
536 profile from the grid image to the orthogonal coordinate sets using ImageJ (NIH). The pre-
537 scribed program then corrected every image tile by calling the ImageJ deformation function
538 using that profile. Afterwards, we used the entire set of imaged tiles (full mouse brain in this
539 case) to map out the tile-wise illumination profile. The images were grouped according to the
540 stage movement, which affects the photo-bleaching profile. The program avoids using pixels that
541 are considered empty background or dura artifacts using preset thresholds. Using those averaged
542 profile tiles, the program normalized all the tile images. Please note, this profile is unique for
543 each sample. Finally, the program picked 16 coronal slices (out of the nearly 2,000) with equal
544 spacing and utilized ImageJ's grid/collection stitching plugin to computationally stitch those 16
545 slides. The program then combined the transformation profiles from center to outer edge
546 according to the calculated pairwise shifting distance. It used a tile-intensity weighted average to
547 ensure the empty tiles did not contribute to the final profile. This approach significantly reduced
548 the computational time and allowed parallelization with no communication overhead. The
549 program automatically performed the aforementioned alignment and stitched the image set
550 together. The program finally aligned the image sets if the sample was imaged through multiple
551 runs during imaging acquisition.

552

553 **Computational: Vessel Digitization/Tracing**

554 We started with interpolating the data into 1x1x1 μ m resolution with cubic interpolation then
555 subtracted the signal color channel (green) with the background color channel (red) to remove

556 auto-fluorescent backgrounds. Next we performed a voxel binarization. The voxel with at least
557 one of the following conditions passed as the foreground signal (vasculature), **a.** the voxel passed
558 a fixed threshold (6x that of the non-empty space average) or **b.** passed a threshold (2.4x that of
559 the non-empty space average) after subtracting a circular 35% local ranking filter. The binarized
560 image was then skeletonized using 26-neighbor rule (Kollmannsberger et al., 2017). The code
561 then reconnected loose ends that were within 10 μm distance and removed all the short stem/furs
562 shorter than 50 μm starting with the short ones and iterated until no more fur artifacts were found
563 (Figure S1F). By using the binary image and the skeleton (center-line), the radius for each
564 skeleton pixel can be measured. The code then grouped all the skeleton pixels into segments with
565 the branching nodes, and all the segments shorter than 2x radius were further cleaned up with
566 shortest graph path (Figure S1G). ROIs with poorly connected ($<250 \mu\text{m}/\text{node}$) were excluded in
567 further analysis as shown Figure S1H. Finally, the code documented and traced all the segments
568 and nodes with their connectivity, length, averaged radius, and raw skeleton locations. The full
569 pipeline here is programmed to be fully automatic and the code was fully vectorized and
570 parallelized with reasonable memory consumption per thread ($\sim 8\text{GB}$).

571

572 **Computational: Fluid Dynamic Simulation**

573 The goal of calculating and visualizing a permeability tensor is to illustrate how well fluid can
574 flow through the local microvasculature of a given volume in a given direction. Since the
575 direction distribution of the microvasculature can be anisotropic, the fluid flow can move with a
576 direction that is different from the pressure gradient direction, thus making the permeability in a
577 tensor form. Such a tensor can illustrate the local microvascular performance and its directional
578 characteristic.

579 The equation of permeability tensor is given by:

$$580 \quad \bar{k} \cdot \nabla P = Q$$

581 or

$$582 \quad \begin{bmatrix} k_{xx} & k_{yx} & k_{zx} \\ k_{xy} & k_{yy} & k_{zy} \\ k_{xz} & k_{yz} & k_{zz} \end{bmatrix} \begin{bmatrix} P_{,x} \\ P_{,y} \\ P_{,z} \end{bmatrix} = \begin{bmatrix} Q_x \\ Q_y \\ Q_z \end{bmatrix}$$

583 where k is the permeability tensor, P is the pressure, Q is the fluid flux, the subscript index is the
584 Cartesian coordinate direction, and the comma is partial differentiation. We chose a size of 400 x
585 400 x 400 μm as the local representative control volume. We then probed the system with three
586 ∇P that are equal to three unit-vector on the Cartesian coordinate. The pressure profile was
587 applied on the surface of the cubical control volume, then the network flow profile was
588 calculated by solving the system of equations of the Hagen–Poiseuille equation (with the
589 viscosity set to unity for normalization) and conservation of flux. We chose the center cut plan to
590 measure the directional flux and consequently, the permeability. Finally, to illustrate the vascular
591 directionality of the isocortex, we projected the tensor onto penetrating, anterior-posterior,
592 medial-lateral vectors according to their location within the isocortex using the equation $k_{pj} =$
593 $|\bar{k} \cdot \mathbf{n}_{pj}|$, where subscript pj indicates the direction of the projecting vessels.

594

595 **Computational: Deep Learning Neural Network (DLNN) pericyte counting**

596 We used a deep learning neural network (DLNN) to detect and classify cells. Instead of using a
597 fully convoluted neural network like Unet, we chose to use per-cell multi-resolution-hybrid
598 ResNet classification with potential cell locations. This makes the AI compute time significantly
599 shorter. The potential cell locations were identified with local maximum within a radius of $r = 8$

600 μm . The image around the potential cell locations was fed to the network with two different
601 resolutions. One is $101 \times 101 \mu\text{m}$ (101×101 pixel) and the other one is $501 \times 501 \mu\text{m}$ (201×201
602 pixel). The two-window system allows the network to capture characteristics from two zoom
603 scales at the same time. In order to use global maximum at the end of the network, we stacked an
604 empty (value zero) image onto the 3D direction of each image, which made them $101 \times 101 \times 2$
605 and $201 \times 201 \times 2$ pixels. We then assigned value 1 to the location of the potential cell, in this
606 case, the center. At the end of the two networks of those two images, the intermediate images
607 were flattened and concatenated into one. The classification was done with two bins, ‘pericytes’
608 and ‘everything else.’ The detailed schematic describing the network is in Figure S4.
609 We deployed two human annotators with the same training to annotate the data, and only used
610 the mutually agreed data to train the AI to eliminate human error and bias. We used a strict set of
611 criteria to include only capillary pericytes that have two subtypes (junctional and helical
612 pericytes). Cells were counted only when the cell body was in the imaging plane and clear
613 pericyte cell morphology could be detected. Cells associated with larger vessels, often with
614 vascular smooth muscle morphology, were not counted to prevent the inclusion of erroneous cell
615 types. We also excluded transitional cell types often referred to as either ensheathing pericytes or
616 precapillary arteriolar smooth muscle cells, due to the controversy in the field as to whether this
617 should be included as a pericyte subtype (Attwell et al., 2016; Grant et al., 2019; Hartmann et al.,
618 2015). A total 12,000 potential cell locations from multiple anatomical regions across 4 different
619 brains were annotated by both annotators. 90% of the data selected at random was used to train
620 the AI and the remaining 10% was used for validation. The 90% of the data taken for training
621 was further truncated down to 3,400 potential cell locations with half positive and half negative
622 for training. The positive cell selections in the raw data were around 19.6% (annotator #1) to
623 21.1% (annotator #2). The validation set was not truncated to represent actual performance. The
624 performance can be found in Table S3.

625 626 **Computational: Deep Learning Neural Network (DLNN) nNOS neuron counting**

627 The morphology and size of tdTomato positive cells in the granular layer of the cerebellum from
628 nNOS-CreER: Ai14 mice differs significantly from other tdTomato positive nNOS neurons in
629 other brain regions. Thus, we developed new DLNN AI algorithms to consider not only cell
630 morphology but also the location of cells by putting additional zoomed-out, low-resolution
631 images of whole coronal sections. The network set-up is similar to the pericyte classification
632 with one more image containing the coronal section with the cell location. The inputs are 101
633 $\times 101 \mu\text{m}$ (101×101 pixel), $501 \times 501 \mu\text{m}$ (201×201 pixel), and the full frame low resolution 12
634 $\times 8 \text{ mm}$ (201×201 pixels). Similar to the pericyte network, we made images $101 \times 101 \times 2$, 202
635 $\times 202 \times 2$, and $202 \times 202 \times 2$ pixels with the cell location marked as value 1. At the end, those
636 three sub-networks were flattened and concatenated into one. The classification is done with
637 three bins, nNOS neurons, cerebellar granular nNOS neurons, and everything else. One human
638 user created 10,000 annotations from 5 nNOS and 5 nNOS subtype brains. 5,000 cells from 5
639 brains were initially used to train the AI. Another 5,000 cells from 5 new brains were used to
640 evaluate the AI performance. The AI reached an F1 score = 0.96, which is comparable to human
641 performance. The details for the network are in Figure S4. The performance can be found in
642 Table S3.

643 644 **Isocortical flatmap**

645 We started with Allen CCF annotation images to solve the Laplace equation by setting the
646 surface of cortical layer 1 as potential '1,' the surface of layer 6b as '0,' and the surface of
647 everything else as flux '0' (Wang et al., 2020). We used the potential map to find the gradient
648 direction as the projecting direction. The projection was first traced to the cortical surface and
649 then flattened at the Anterior-Posterior (A-P) tangential plane, which later preserved the A-P
650 coordinate on the flat map. The flattened map has the y-axis mapped as the original A-P
651 coordinate at the surface, and the x-axis was adjusted to represent the surface arc (azimuth)
652 length to the reference X-zero. The reference X-zero was defined on the cortical ridge in the
653 dorsal direction (maximum Y point in 3D) with a straight cut in the A-P direction. Finally, the
654 projection profile was saved at two resolutions, $10 \times 10 \times 10 \mu\text{m}^3$ and $20 \times 20 \times 20 \mu\text{m}^3$. We
655 created a Matlab script that can map any signals (previously registered to the Allen CCF) into a
656 3D projected isocortical flatmap.

657

658 **Conversion of 2D based counting to 3D cell density**

659 STPT imaging has very accurate cutting and stage depth movement, which allows us to convert
660 the 2D cell counting to 3D cell density. We used previously calculated 3D conversion factors for
661 cytoplasmic (factor = 1.4) and nuclear signals (factor = 1.5) to generate density estimates of
662 nNOS neurons and other neuronal cell type datasets (Kim et al., 2017). To estimate the 3D
663 conversion factor for pericytes, we imaged one PDGFR β -Cre: Ai14 mouse brain with $1 \times 1 \times 5$
664 μm , as done with vascular imaging (Figure 1B). Then, we applied our pericyte cell counting in
665 all images from this densely imaged dataset. Since the DLNN cell counting was done in 2D, the
666 same cell can be counted more than once in adjacent z stack images. We resolved this issue by
667 compiling the counting into a $5 \times 5 \times 5 \mu\text{m}^3$ resolution 3D array, dilating the mask by 1 pixel,
668 and counting the connected pieces, which avoids over counting any cell that is within 25 μm
669 proximity. This 3D counting result was then compared to the 2D counting from the 5th section
670 from every ten z optical image stack (Figure 1B). The calculated 3D/2D ratio was 3.33 for
671 pericytes, which was applied as a conversion factor to estimate pericyte numbers in 3D.
672 To estimate the anatomical volume from each sample, the Allen CCF was registered to
673 individual samples first using Elastix (Klein et al., 2010). Anatomical labels were
674 transformed based on the registration parameters and the number of voxels associated with
675 specific anatomical IDs were used to estimate the 3D volume of each anatomical area (Kim et
676 al., 2017).

677

678 **In vivo two-photon recording and comparison with STPT vascular measurement**

679 *Surgery.* All surgeries were performed under isoflurane anesthesia (in oxygen, 5% for induction
680 and 1.5-2% for maintenance). A custom-machined titanium head bolt was attached to the skull
681 with cyanoacrylate glue (#32002, Vibra-tite). The head bolt was positioned along the midline
682 and just posterior to the lambda cranial suture. Two self-tapping 3/32" #000 screws (J.I. Morris)
683 were implanted into the skull contralateral to the measurement sites over the frontal lobe and
684 parietal lobe. For measurements using two-photon laser scanning microscopy (2PLSM), a
685 polished and reinforced thin-skull (PoRTS) window was made covering the right somatosensory
686 cortex as described previously (Drew et al., 2010; Zhang et al., 2019a). Following the surgery,
687 mice were returned to their home cage for recovery for at least one week, and then started
688 habituation on experimental apparatus. Habituation sessions were performed 2-4 times over the
689 course of one week, with the duration increasing from 5 min to 45 min.

690 **Measurements using two-photon laser scanning microscopy (2PLSM).** Mice were briefly
691 anesthetized with isoflurane (5% in oxygen) and retro-orbitally injected with 50 μ L 5%
692 (weight/volume in saline) fluorescein-conjugated dextran (70 kDa, Sigma-Aldrich, cat.no.:
693 46945), and then fixed on a spherical treadmill. Imaging was done on a Sutter Movable
694 Objective Microscope with a 20X, 1.0 NA water dipping objective (Olympus, XLUMPlanFLN).
695 A MaiTai HP (Spectra-Physics, Santa Clara, CA) laser tuned to 800 μ m was used for
696 fluorophore excitation. All imaging with the water-immersion lens was done with room
697 temperature distilled water between the PoRTS window and the objective. All the 2PLSM
698 measurements were started at least 20 minutes after isoflurane exposure to reduce the disruption
699 of physiological signals due to anesthetics (Gao et al., 2017). High-resolution image stacks of the
700 vasculature were collected across a 500 by 500 μ m field and up to a depth of 250 μ m from the
701 pial surface. All the images were acquired with increasing laser power up to 100 mW at a depth
702 of \sim 200 μ m. Lateral sampling was 0.64 μ m per pixel and axial sampling was at 1 μ m steps
703 between frames. Shortly (within 20 minutes) after the imaging, the mouse was perfused with
704 FITC filling for STPT based *ex vivo* vasculature imaging.

705

706 **In vivo and ex vivo comparison.**

707 In order to compare our measurements for vessel radii in STPT imaging datasets to vessel
708 parameters measured *in vivo*, the same animals that were used for 2PLSM (See **In vivo two-**
709 **photon recording and comparison with STPT vascular measurement**) underwent the FITC-
710 fill perfusion and STPT imaging steps described above. However, STPT imaging was only
711 conducted on the cortical hemisphere used for 2PLSM, with imaging spanning from prefrontal
712 regions to visual cortex regions, in order to appropriately capture the primary somatosensory
713 cortex limb region. Following stitching and tracing of the images, the raw imaging data was 3D
714 reconstructed in order to visualize the cortical surface. To find the 2PLSM imaging window,
715 vessel landmarks used to reimage in 2PLSM were again used to identify the same landmark
716 vessels in the STPT imaging dataset (Figure S2). The region of interest was further confirmed by
717 anatomical landmarks (proximity to bregma, surface vessels, etc.) through overlay of STPT and
718 2PLSM imaging window regions. Next, within a STPT imaging z stack, borders were inserted
719 using ImageJ software to further outline the *in vivo* imaging window region in the 3D data. Then
720 the *in vivo* imaging z stack data were used to identify branch points along the penetrating vessel
721 tracked during 2PLSM. This provided identifiable characteristics to further locate the same
722 vessel in the STPT imaging dataset. Once the exact vessel was identified in the STPT images, the
723 precise 3D coordinates were tracked to accurately obtain the radii measurements from the traced
724 vessel data, see the **Computational: Vessel Digitization/Tracing** section for details. In 2PLSM
725 images, vessel diameter measurements were manually taken with adjusted pixel/micron distances
726 using the straight-line function in ImageJ. These vessel diameter measurements accounted for the
727 lumen of the vessel, at half of the maximum fluorescence intensity profile and were adjusted for
728 pixelation of 2PLSM data. These measurements have been further refined through VasoMetrics
729 ImageJ macro (McDowell et al., 2021). To identify the radii and diameter measurements from
730 the STPT imaging data, exact vessel coordinates were used to retrieve the associated vessel radii
731 measurements using custom MATLAB code. A minimum of 10 vessel diameter measurements
732 were taken per imaging window (each animal contained 2 imaging regions of interest) per
733 animal.

734

735

736 **Statistical analysis**

737 All statistical analysis, including multi-region of interest (ROI) correlation analysis, was done in
738 Matlab (Mathworks). We used an averaged value of the experimented animals while treating
739 each ROI as an individual data point to calculate the correlation coefficient R between vascular
740 and cell density measurements. The p value was calculated based on the null hypothesis that the
741 two groups have no correlation; the values were adjusted with the Bonferroni correction for
742 multiple comparison correction.
743

744 **Acknowledgments**

745 This publication was made possible by an NIH grant R01NS108407 to Y.K., R01NS078168 and
746 R01NS101353 to P.J.D. Its contents are solely the responsibility of the authors and do not
747 necessarily represent the views of the funding agency. We thank Dr. Volkhard Linder for kindly
748 sharing PDGFR β -Cre transgenic mice and Rebecca Betty for assistance in editing the
749 manuscript. We acknowledge use of computational resources in the High Performance
750 Computing cluster at the Penn State College of Medicine.

751

752

753

754 **Contributions**

755 Conceptualization, Y.K.; Data Collection, H.C.B, U.C., Y.K.; Developing Computational
756 Analysis, Y.W.; Data Analysis, Y.W., H.C.B., U.C.; In vivo two-photon imaging, Q.Z.,
757 P.J.D.; Neuronal subtypes STPT data collection; R.M., P.O.; Web visualization, D.J.V., K.C.;
758 Manuscript preparation: Y.K., Y.W., H.C.B. with help from other authors.

759

760

761 **Competing Interests**

762 The authors declare no competing interests.

763

764

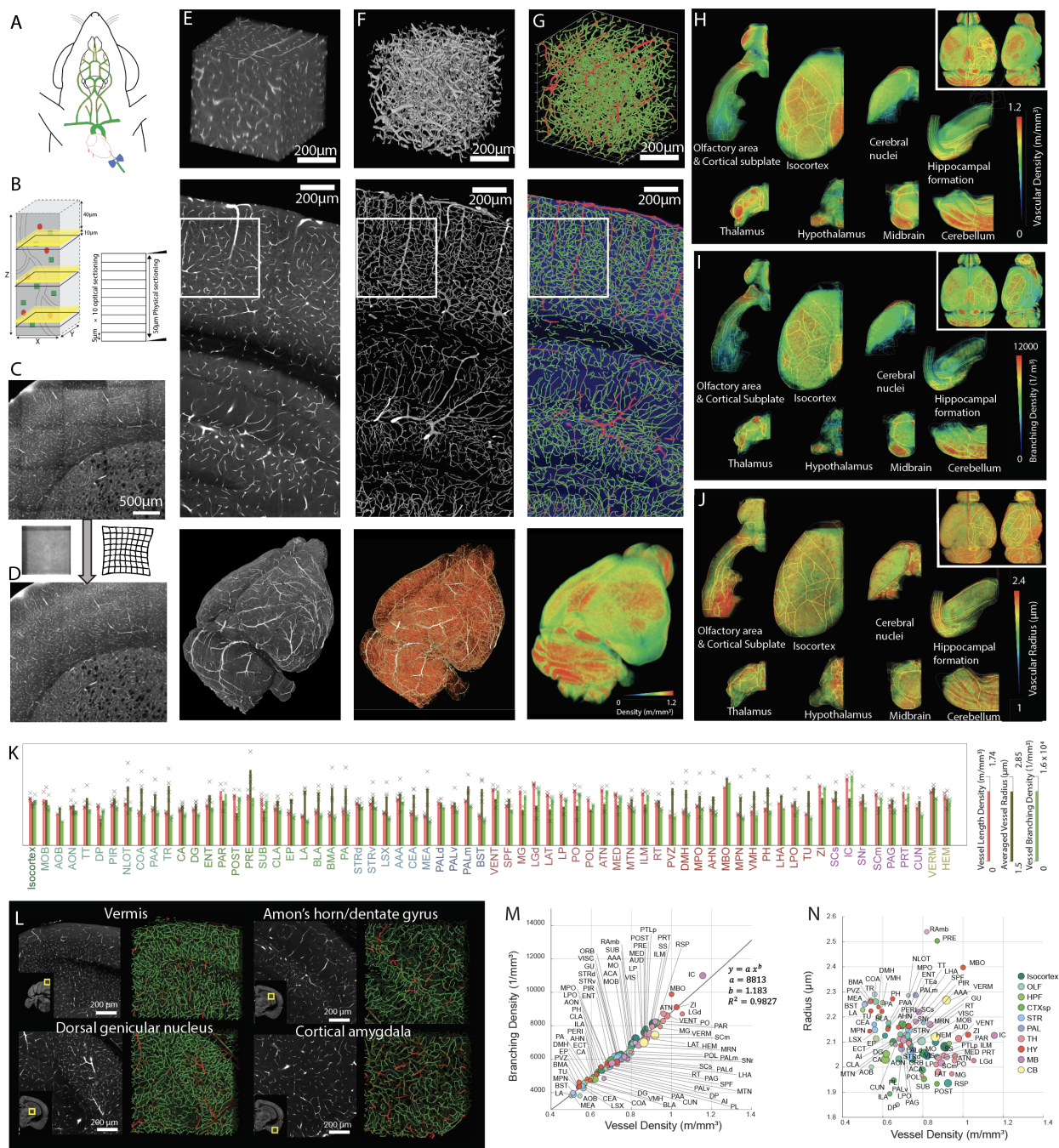
765 **Data Sharing Plan**

766 High-resolution serial two-photon tomography images can be found at [https://kimlab.io/brain-](https://kimlab.io/brain-map/nvu/)
767 [map/nvu/](https://kimlab.io/brain-map/nvu/)

768 Custom-built codes including isocortical flatmaps are available as Supplementary data (Code S1-
769 S3)

770

771

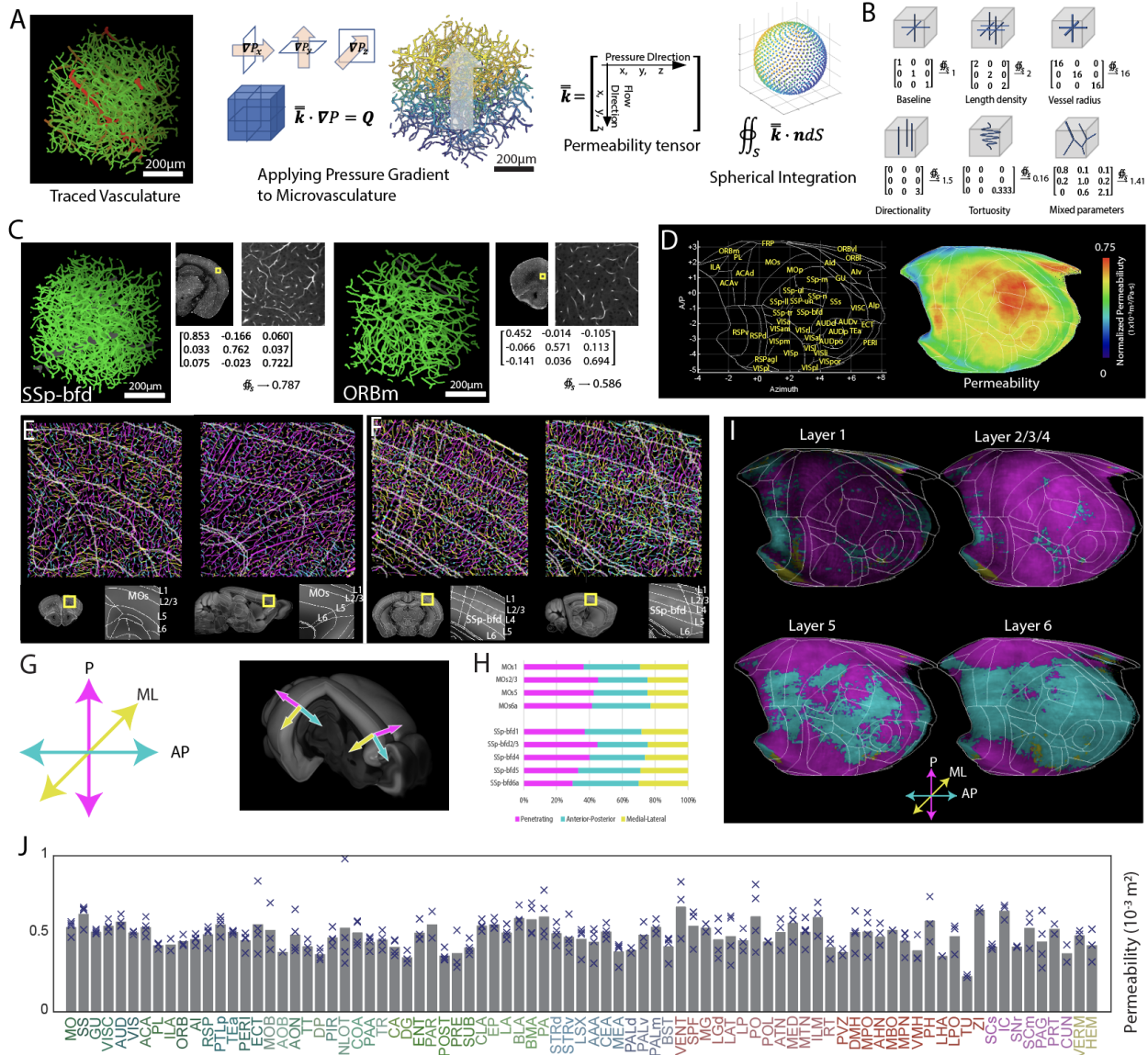


772
773

774 **Figure 1. High resolution 3D mapping of the entire vasculature in the mouse brain.**
 775 **A.** Fluorescent dye (FITC)-conjugated albumin gel perfusing the mouse brain through the heart
 776 to label cerebrovasculature. **B.** Combination of physical sectioning (vibratome cutting) and
 777 optical sectioning to achieve lossless imaging of a sample. Left: black-plane indicates the
 778 physical cuts, yellow-zones indicates an optical sectioning imaging plane. Right: 10 optical
 779 imaging sections per one physical sectioning. **C-D.** Stitching with optical aberration and tile line
 780 correction (**D**) from uncorrected images (**C**). **E-G.** Example outputs from each stage of the
 781 analysis pipeline. Top row: 100 μm thick 3D volume from the white box area from the middle
 782 row, Middle row: An example coronal section, Bottom row: The whole brain results. **E.** The raw

783 image volume of FITC labeled vasculature. **F.** The binarized vasculature. **G.** The traced
784 vasculature. Large (radius > 5 μm) and small vessels are colored as red and green, respectively in
785 the top and middle image. The bottom image shows the vasculature density. **H-J.** The averaged
786 vasculature length density (H), branching density (I), and radii (J) from four brains are registered
787 to the Allen CCF and displayed with heatmap in 8 major areas across the whole mouse brain. **K.**
788 Average vessel density, radius, and branching density across the whole brain. Individual animal
789 data that pass the tracing quality control as shown in Figure S1 are shown as X. See also Table
790 S1. **L.** Examples of areas with different vasculature density and radii. **M-N.** The correlation
791 between vessel density and branching density (M) and the correlation between vessel density and
792 the averaged radius (N). Size of each ROI is displayed according to relative volume of the area.
793 Note strong correlation between vessel density with branching density, but not with vascular
794 radii.
795

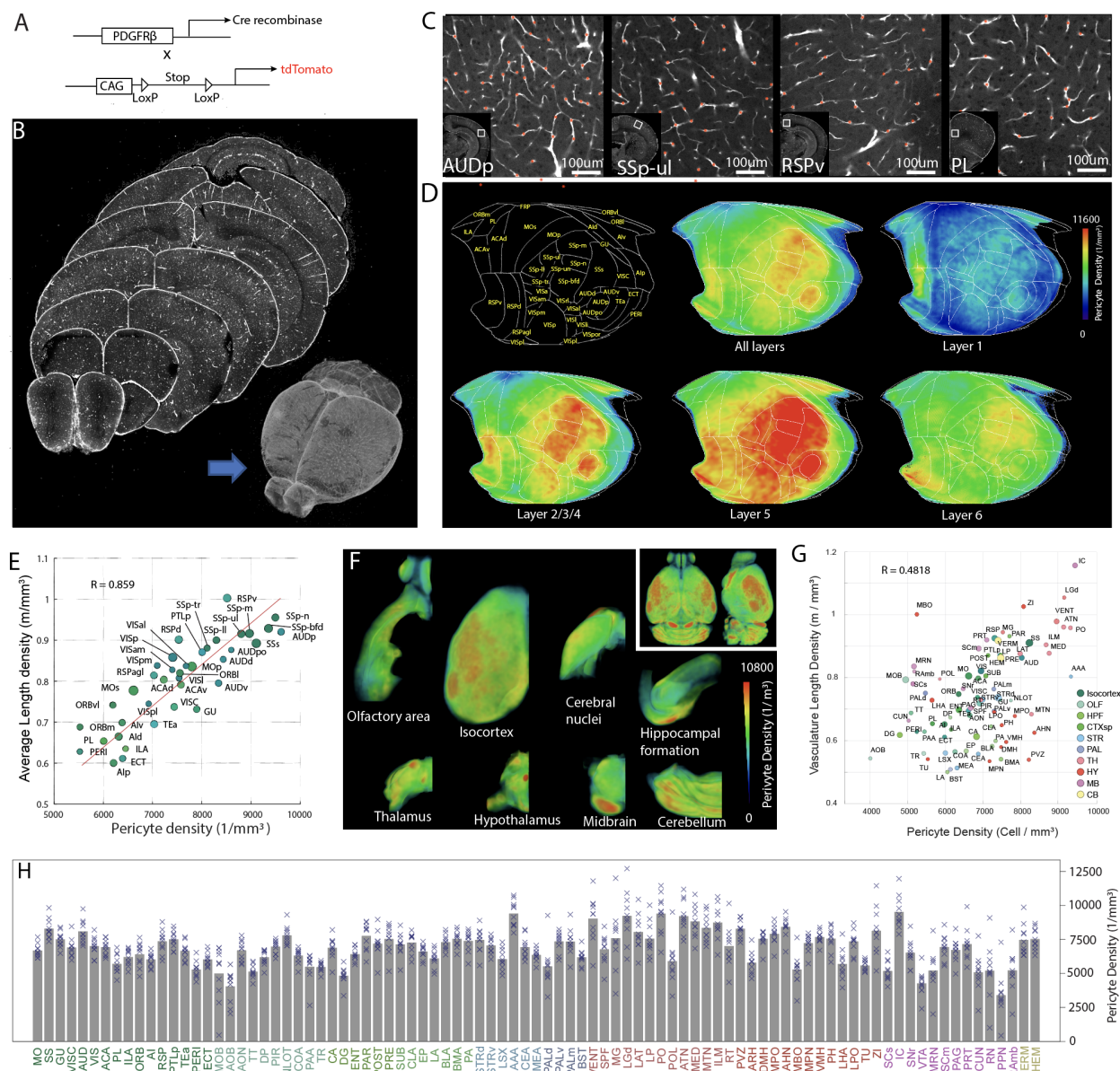
809 and retrosplenial (black arrowhead) cortex, while there is a low density in lateral association
810 cortex (white arrow). **H.** Cortical layer specific max projection of vasculature length density.
811
812



813
814

Figure 3. Anisotropy of the cerebral microvascular network and its impact on permeability
A. The flow chart of the permeability fluid dynamic simulation. From left to right: Original
traced data, applying pressure profile on the surface of the control volume with a gradient profile
and solving the coincide flux equation set for the permeability tensor, the annotation rule of the
permeability tensor, and the sampling dots of the numerical spherical integration. Equation
symbols: l : perfusing length, P : pressure, Q : Blood flux, R : resistance, μ : viscosity, k :
permeability, Δ : changing of the quantity, \cdot : dot product, ∇ : gradient, \oint_S : spherical integral, S :
spherical surface, n : normal direction, bold-font: vector, double-top-bar: tensor. **B.** Examples
illustrating how the structure of the vasculature network impacts the permeability tensor. **C.** Two
examples of the real network with its permeability tensor from primary somatosensory, barrel
field (SSp-bfd), and medial orbital cortex (ORBm). **D.** Spherically integrated permeability results
in the cortical flatmap. **E-F.** Microvessel anisotropy measurement in the isocortex. Examples
from the motor cortex (E) and somatosensory (F) cortices. **G.** Microvessels in (E-F) are colored
based on its directionality; magenta for penetrating (P), cyan for anterior-posterior (AP), yellow

829 for medial-lateral (ML). Directionality axis is based on cortical column angles in each area. **H.**
830 Permeability measurement of the secondary motor cortex (MOs) and the SSp-bfd in the three
831 directionalities. **I.** Microvessel directionality in cortical layers. Only the dominant direction is
832 displayed for simplicity. **J.** Permeability results of the whole brain. See also Table S2.
833
834



835
836

837 **Figure 4: Pericyte density mapping across the whole mouse brain**

838 **A.** Schematic depicting genetic construct for PDGFR β -Cre:tdTomato mouse model. **B.**

839 Representative coronal images and a reconstructed brain from the STPT imaging of a PDGFR β -

840 Cre:tdTomato mouse. **C.** Example images of areas showing variability in pericyte density. High

841 pericyte density in the auditory (top left) and somatosensory cortex (top right) while low density

842 in the prelimbic (bottom left) and retrosplenial cortex (bottom right). **D.** Cortical flatmap of

843 averaged pericyte density across the isocortex by cortical layer. **E.** Scatter plot demonstrating

844 significantly positive correlation between pericyte density and vascular length density in

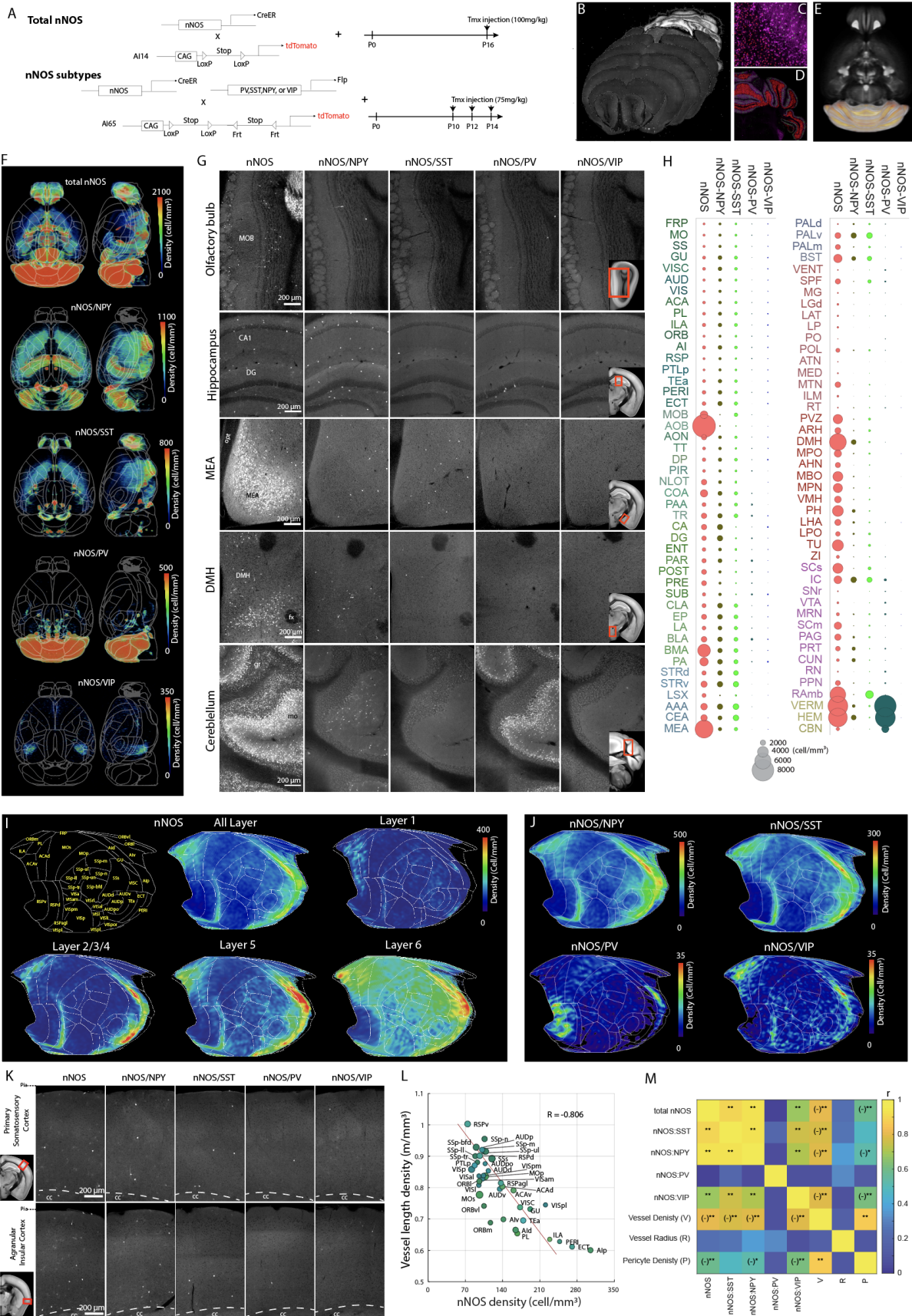
845 isocortical regions ($R=0.859$, p value = 1.86×10^{-12}). **F.** Heat maps of pericyte density distribution

846 across the adult brain. **G.** Scatterplot comparison of average vessel length density and pericyte

847 density across all brain regions shows significant correlation ($R=0.4818$, p value = 2.65×10^{-6}).

848 **H.** Quantifications of pericyte density across all brain regions. Brain regions are color coded to

849 match the regions represented in (G). See also Table S4.

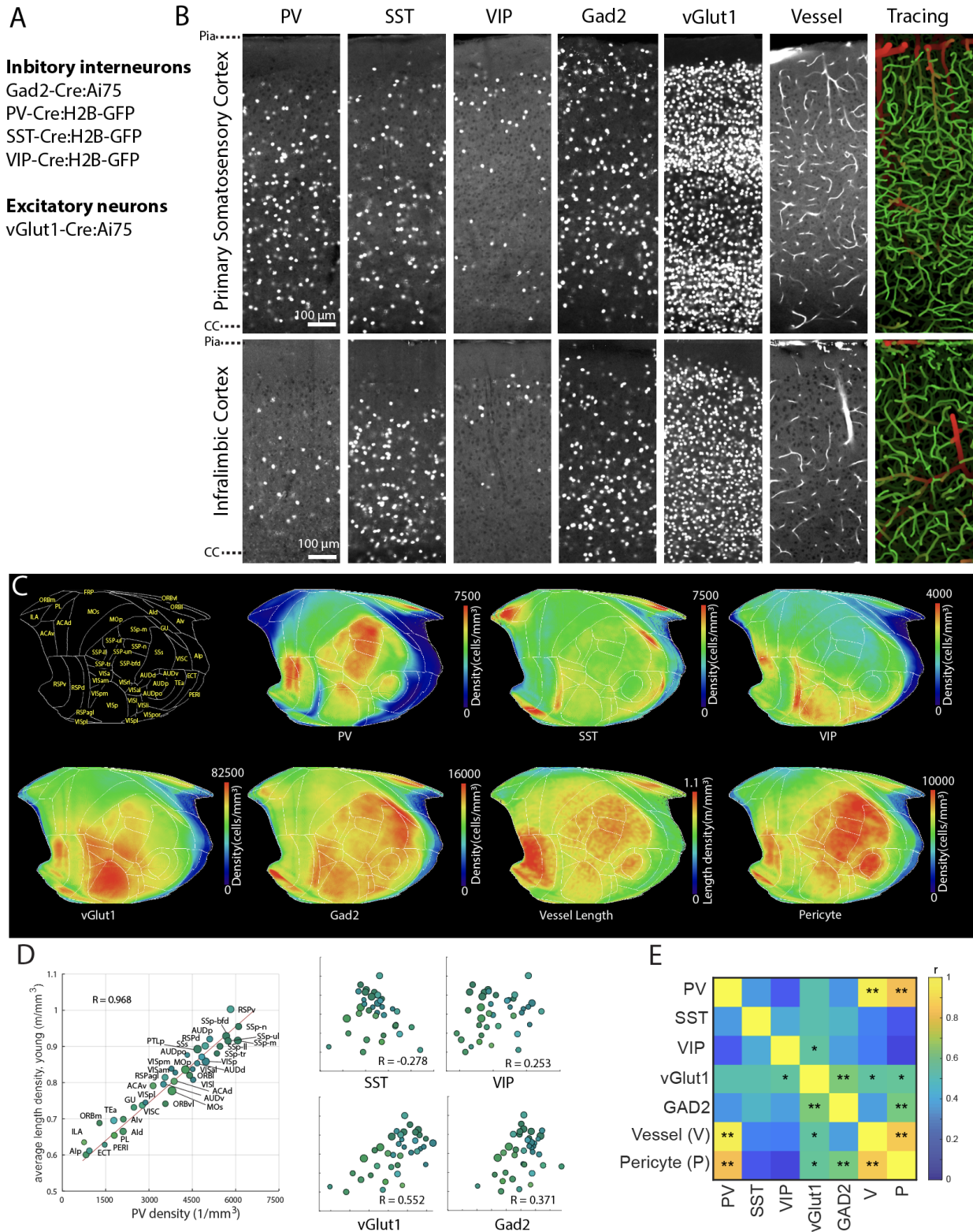


851 **Figure 5: Brain-wide density map of nNOS neurons and their subtypes**

852 **A.** Cell type-specific transgenic mice with tamoxifen treatments to label either total nNOS
853 neurons or nNOS subtypes co-expressing NPY, SST, PV, or VIP. **B.** Coronal section examples
854 from STPT Imaging of a nNOS: Ai14 mouse. **C-E.** AI based detection of nNOS cells with two
855 distinct shapes. High resolution image (C) showing nNOS neurons in the molecular (green) and
856 granular cell layer (red) of the cerebellum (D). **E.** Representative image of total nNOS
857 population throughout the brain. **F.** Heat maps demonstrating the distribution of total nNOS and
858 nNOS subtype populations. See also Movie S4 and Table S5. **G.** Representative raw images of
859 nNOS, nNOS/NPY, nNOS/SST, nNOS/PV and nNOS/VIP neurons in the olfactory bulb,
860 hippocampus, medial amygdala (MEA), dorsomedial hypothalamus (DMH) and cerebellum.
861 Reference atlas images included on nNOS/VIP images show the area displayed for each region
862 of interest. Main olfactory bulb (MOB), Ammon's horn (CA1), dentate gyrus (DG), optic tract
863 (opt), fornix (fx), granular (gr), molecular (mo). **H.** Graph showing nNOS density by brain
864 region for the total nNOS neurons and their subtypes. Size of circle corresponds to density as
865 shown in the key at the bottom. **I-J.** Isocortical flatmap for averaged density of total nNOS
866 neurons by layer (I) and overall density of nNOS subtypes in the isocortex (J). Note higher
867 nNOS density in the medial prefrontal and lateral association areas. **K.** Representative STPT
868 images of nNOS cell types from the primary somatosensory cortex and the agranular insular
869 cortex. **L.** Scatter plot showing significant negative correlation between total nNOS density and
870 vessel length density in the isocortex (R value = -0.806, p value = 6.9×10^{-7}). **M.** Correlation
871 matrix between nNOS cell types and vascular/pericyte measurements. *p<0.05, **p<0.005 after
872 the Bonferroni correction. (-) denote negative correlation.

873

874



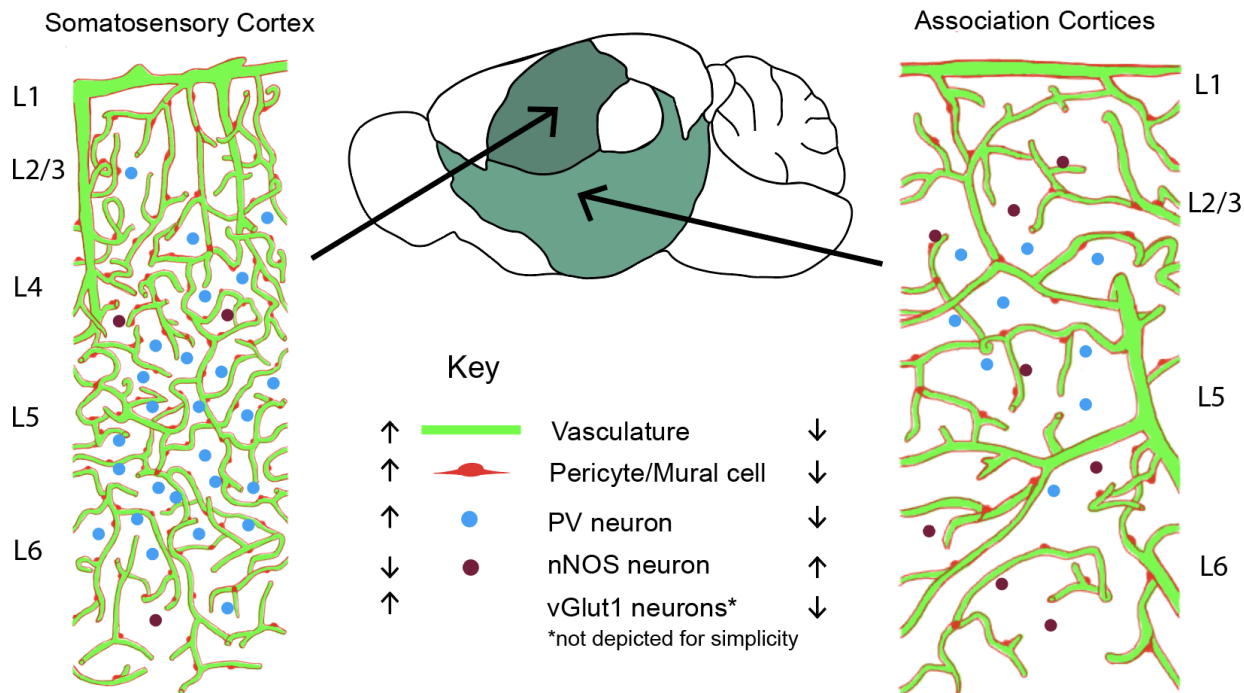
875
 876
 877
 878

Figure 6: Cortical parvalbumin and vGlut1 neurons positively correlated with vasculature density

879 **A.** Cell type-specific labeling of neurons to visualize cortical inhibitory interneuron and
880 excitatory neuron populations. **B.** Distribution of inhibitory interneurons, excitatory neurons, and
881 the vasculature and its tracing result (large vessels=red, microvasculature=green) from the
882 densely vascularized primary somatosensory and sparsely vascularized infralimbic cortices. **C.**
883 Cortical flatmap showing density distributions of neuronal subtypes as well as vessel length and
884 pericyte densities. **D.** Correlation between vascular density and neuronal subtypes. Note very
885 strong positive correlation with PV density ($R = 0.968$, p value = 8.5×10^{-22}) and positive
886 correlation with vGlut1 excitatory neuronal density ($R = 0.552$, p value = 5.9×10^{-3}). **E.**
887 Correlation matrix between neuronal subtypes, vessel length density and pericyte density.
888 * $p < 0.05$, ** $p < 0.005$ after the Bonferroni correction.

889

890



891
892
893
894
895
896
897
898

Figure 7: Cortical organization of the vascular/pericyte network and neuronal cell types

Sensory cortices including the somatosensory cortex are characterized by relatively high density of vessels, pericytes, PV interneurons, and vGlut1 excitatory neurons, and a low density of nNOS neurons. In contrast, association cortices show the opposite pattern.

Region of Interest	Vessel length density (m/mm ³)	Pericyte (cell/mm ³)	nNOS neurons (cell/mm ³)	PV neurons (cell/mm ³)	vGlut neurons (cell/mm ³)
Motor	0.81 ± 0.05	6,603 ± 489	104 ± 17	2,678 ± 203	35,566 ± 823
Somatosensory	0.91 ± 0.07	8,208 ± 739	108 ± 16	3,664 ± 281	45,022 ± 838
Auditory	0.86 ± 0.06	8,006 ± 848	121 ± 16	2,965 ± 295	42,178 ± 1,676
Visual	0.82 ± 0.07	6,930 ± 697	112 ± 22	2,927 ± 352	49,329 ± 1,132
Retrosplenial	0.92 ± 0.07	7,290 ± 869	103 ± 20	3,330 ± 387	44,631 ± 2,494
Posterior Parietal	0.87 ± 0.07	7,428 ± 641	91 ± 17	3,220 ± 255	47,030 ± 875
Orbital	0.75 ± 0.08	6,338 ± 891	106 ± 17	2,290 ± 320	38,014 ± 1,559
Anterior Cingulate	0.8 ± 0.05	6,856 ± 555	154 ± 32	2,371 ± 213	41,208 ± 1,039
Prelimbic	0.65 ± 0.04	5,645 ± 726	171 ± 34	1,199 ± 171	39,270 ± 1,098
Infralimbic	0.64 ± 0.02	6,139 ± 602	232 ± 38	503 ± 120	43,679 ± 1,973
Visceral	0.74 ± 0.04	6,837 ± 689	177 ± 33	1,846 ± 204	37,081 ± 1,546
Gustatory	0.73 ± 0.03	7,421 ± 581	194 ± 34	1,652 ± 212	40,783 ± 1,467
Agranular Insular	0.65 ± 0.05	5,966 ± 500	207 ± 41	1,154 ± 118	31,290 ± 1,023
Perirhinal	0.63 ± 0.03	5,232 ± 615	265 ± 69	979 ± 142	24,789 ± 3,196
Temporal Association	0.7 ± 0.04	6,596 ± 639	187 ± 37	1,189 ± 210	42,407 ± 1,907
Ectorhinal	0.61 ± 0.02	5,967 ± 510	283 ± 63	623 ± 117	38,578 ± 3,400

899

900 **Table 1: Density of the cerebrovasculature, pericytes, and neuronal subtypes in the**
 901 **isocortex**

902 Number = average ± standard deviation, see Table S1, S3, S5, S6 for full dataset.

903 **References**

904

905 Attwell, D., Buchan, A.M., Charpak, S., Lauritzen, M., Macvicar, B.A., and Newman, E.A.
906 (2010). Glial and neuronal control of brain blood flow. *Nature* *468*, 232–243.

907 Attwell, D., Mishra, A., Hall, C.N., O’Farrell, F.M., and Dalkara, T. (2016). What is a pericyte?
908 *J Cereb Blood Flow Metab* *36*, 451–455.

909 Ballinger, E.C., Ananth, M., Talmage, D.A., and Role, L.W. (2016). Basal Forebrain Cholinergic
910 Circuits and Signaling in Cognition and Cognitive Decline. *Neuron* *91*, 1199–1218.

911 Balogh, P., and Bagchi, P. (2019). Three-dimensional distribution of wall shear stress and its
912 gradient in red cell-resolved computational modeling of blood flow in in vivo-like microvascular
913 networks. *Physiological Reports* *7*, e14067.

914 Bennett, H.C., and Kim, Y. (2021). Pericytes Across the Lifetime in the Central Nervous System.
915 *Front. Cell. Neurosci.* *15*.

916 Blinder, P., Shih, A.Y., Rafie, C., and Kleinfeld, D. (2010). Topological basis for the robust
917 distribution of blood to rodent neocortex. *Proc Natl Acad Sci U S A* *107*, 12670–12675.

918 Blinder, P., Tsai, P.S., Kaufhold, J.P., Knutsen, P.M., Suhl, H., and Kleinfeld, D. (2013). The
919 cortical angiome: an interconnected vascular network with noncolumnar patterns of blood flow.
920 *Nature Neuroscience* *16*, 889–897.

921 Boido, D., Rungta, R.L., Osmanski, B.-F., Roche, M., Tsurugizawa, T., Le Bihan, D., Ciobanu,
922 L., and Charpak, S. (2019). Mesoscopic and microscopic imaging of sensory responses in the
923 same animal. *Nat Commun* *10*, 1110.

924 Buzsáki, G., Kaila, K., and Raichle, M. (2007). Inhibition and brain work. *Neuron* *56*, 771–783.

925 Cardin, J.A., Carlén, M., Meletis, K., Knoblich, U., Zhang, F., Deisseroth, K., Tsai, L.-H., and
926 Moore, C.I. (2009). Driving fast-spiking cells induces gamma rhythm and controls sensory
927 responses. *Nature* *459*, 663–667.

928 Chachlaki, K., Malone, S.A., Qualls-Creekmore, E., Hrabovszky, E., Münzberg, H., Giacobini,
929 P., Ango, F., and Prevot, V. (2017). Phenotyping of nNOS neurons in the postnatal and adult
930 female mouse hypothalamus. *J. Comp. Neurol.* *525*, 3177–3189.

931 Cuttler, A.S., LeClair, R.J., Stohn, J.P., Wang, Q., Sorenson, C.M., Liaw, L., and Lindner, V.
932 (2011). Characterization of Pdgfrb-Cre transgenic mice reveals reduction of ROSA26 reporter
933 activity in remodeling arteries. *Genesis (New York, N.Y. : 2000)* *49*, 673–680.

934 Devonshire, I.M., Papadakis, N.G., Port, M., Berwick, J., Kennerley, A.J., Mayhew, J.E.W., and
935 Overton, P.G. (2012). Neurovascular coupling is brain region-dependent. *Neuroimage* *59*, 1997–
936 2006.

- 937 Douglas, R.J., and Martin, K.A.C. (2004). Neuronal circuits of the neocortex. *Annu Rev*
938 *Neurosci* 27, 419–451.
- 939 Drew, P.J., Shih, A.Y., Driscoll, J.D., Knutsen, P.M., Blinder, P., Davalos, D., Akassoglou, K.,
940 Tsai, P.S., and Kleinfeld, D. (2010). Chronic optical access through a polished and reinforced
941 thinned skull. *Nat Methods* 7, 981–984.
- 942 Drew, P.J., Mateo, C., Turner, K.L., Yu, X., and Kleinfeld, D. (2020). Ultra-slow Oscillations in
943 fMRI and Resting-State Connectivity: Neuronal and Vascular Contributions and Technical
944 Confounds. *Neuron* 107, 782–804.
- 945 Echagarruga, C.T., Gheres, K.W., Norwood, J.N., and Drew, P.J. (2020). nNOS-expressing
946 interneurons control basal and behaviorally evoked arterial dilation in somatosensory cortex of
947 mice. *Elife* 9.
- 948 Gao, Y.-R., Ma, Y., Zhang, Q., Winder, A.T., Liang, Z., Antinori, L., Drew, P.J., and Zhang, N.
949 (2017). Time to wake up: Studying neurovascular coupling and brain-wide circuit function in the
950 un-anesthetized animal. *NeuroImage* 153, 382–398.
- 951 Grant, R.I., Hartmann, D.A., Underly, R.G., Berthiaume, A.-A., Bhat, N.R., and Shih, A.Y.
952 (2019). Organizational hierarchy and structural diversity of microvascular pericytes in adult
953 mouse cortex. *Journal of Cerebral Blood Flow and Metabolism : Official Journal of the*
954 *International Society of Cerebral Blood Flow and Metabolism* 39, 411–425.
- 955 Hall, C.N., Klein-Flügge, M.C., Howarth, C., and Attwell, D. (2012). Oxidative phosphorylation,
956 not glycolysis, powers presynaptic and postsynaptic mechanisms underlying brain information
957 processing. *J Neurosci* 32, 8940–8951.
- 958 Hall, C.N., Reynell, C., Gesslein, B., Hamilton, N.B., Mishra, A., Sutherland, B.A., O’Farrell,
959 F.M., Buchan, A.M., Lauritzen, M., and Attwell, D. (2014). Capillary pericytes regulate cerebral
960 blood flow in health and disease. *Nature* 508, 55–60.
- 961 Han, Y., Kebschull, J.M., Campbell, R.A.A., Cowan, D., Imhof, F., Zador, A.M., and Mrsic-
962 Flogel, T.D. (2018). The logic of single-cell projections from visual cortex. *Nature* 556, 51–56.
- 963 Hartmann, D.A., Underly, R.G., Grant, R.I., Watson, A.N., Lindner, V., and Shih, A.Y. (2015).
964 Pericyte structure and distribution in the cerebral cortex revealed by high-resolution imaging of
965 transgenic mice. *Neurophotonics* 2, 041402.
- 966 Hartmann, D.A., Berthiaume, A.-A., Grant, R.I., Harrill, S.A., Koski, T., Tieu, T., McDowell,
967 K.P., Faino, A.V., Kelly, A.L., and Shih, A.Y. (2021). Brain capillary pericytes exert a
968 substantial but slow influence on blood flow. *Nat Neurosci*.
- 969 He, M., Tucciarone, J., Lee, S., Nigro, M.J., Kim, Y., Levine, J.M., Kelly, S.M., Krugikov, I.,
970 Wu, P., Chen, Y., et al. (2016). Strategies and Tools for Combinatorial Targeting of GABAergic
971 Neurons in Mouse Cerebral Cortex. *Neuron*.

- 972 Herculano-Houzel, S. (2011). Scaling of Brain Metabolism with a Fixed Energy Budget per
973 Neuron: Implications for Neuronal Activity, Plasticity and Evolution. *PLOS ONE* 6, e17514.
- 974 Hill, R.A., Tong, L., Yuan, P., Murikinati, S., Gupta, S., and Grutzendler, J. (2015). Regional
975 Blood Flow in the Normal and Ischemic Brain Is Controlled by Arteriolar Smooth Muscle Cell
976 Contractility and Not by Capillary Pericytes. *Neuron* 87, 95–110.
- 977 Hosford, P.S., and Gourine, A.V. (2019). What is the key mediator of the neurovascular coupling
978 response? *Neurosci Biobehav Rev* 96, 174–181.
- 979 Howarth, C., Gleeson, P., and Attwell, D. (2012). Updated energy budgets for neural
980 computation in the neocortex and cerebellum. *J Cereb Blood Flow Metab* 32, 1222–1232.
- 981 Howarth, C., Mishra, A., and Hall, C.N. (2021). More than just summed neuronal activity: how
982 multiple cell types shape the BOLD response. *Philos Trans R Soc Lond B Biol Sci* 376,
983 20190630.
- 984 Hu, H., and Jonas, P. (2014). A supercritical density of Na⁺ channels ensures fast signaling in
985 GABAergic interneuron axons. *Nature Neuroscience* 17, 686–693.
- 986 Huo, B.-X., Smith, J.B., and Drew, P.J. (2014). Neurovascular coupling and decoupling in the
987 cortex during voluntary locomotion. *Journal of Neuroscience* 34, 10975–10981.
- 988 Inan, M., Zhao, M., Manuszak, M., Karakaya, C., Rajadhyaksha, A.M., Pickel, V.M., Schwartz,
989 T.H., Goldstein, P.A., and Manfredi, G. (2016). Energy deficit in parvalbumin neurons leads to
990 circuit dysfunction, impaired sensory gating and social disability. *Neurobiol Dis* 93, 35–46.
- 991 Ji, X., Ferreira, T., Friedman, B., Liu, R., Liechty, H., Bas, E., Chandrashekar, J., and Kleinfeld,
992 D. (2021). Brain microvasculature has a common topology with local differences in geometry
993 that match metabolic load. *Neuron*.
- 994 Kann, O. (2016). The interneuron energy hypothesis: Implications for brain disease. *Neurobiol*
995 *Dis* 90, 75–85.
- 996 Kaplan, L., Chow, B.W., and Gu, C. (2020). Neuronal regulation of the blood-brain barrier and
997 neurovascular coupling. *Nat Rev Neurosci* 21, 416–432.
- 998 Kepecs, A., and Fishell, G. (2014). Interneuron cell types are fit to function. *Nature* 505, 318–
999 326.
- 1000 Kim, Y., Yang, G.R., Pradhan, K., Venkataraju, K.U., Bota, M., García Del Molino, L.C.,
1001 Fitzgerald, G., Ram, K., He, M., Levine, J.M., et al. (2017). Brain-wide Maps Reveal
1002 Stereotyped Cell-Type-Based Cortical Architecture and Subcortical Sexual Dimorphism. *Cell*
1003 171, 456-469.e22.
- 1004 Kirst, C., Skriabine, S., Vieites-Prado, A., Topilko, T., Bertin, P., Gerschenfeld, G., Verny, F.,
1005 Topilko, P., Michalski, N., Tessier-Lavigne, M., et al. (2020). Mapping the Fine-Scale
1006 Organization and Plasticity of the Brain Vasculature. *Cell* 0.

- 1007 Klein, S., Staring, M., Murphy, K., Viergever, M.A., and Pluim, J.P.W. (2010). elastix: a toolbox
1008 for intensity-based medical image registration. *IEEE Transactions on Medical Imaging* 29, 196–
1009 205.
- 1010 Kollmannsberger, P., Kerschnitzki, M., Repp, F., Wagermaier, W., Weinkamer, R., and Fratzl, P.
1011 (2017). The small world of osteocytes: connectomics of the lacuno-canalicular network in bone.
1012 *New J. Phys.* 19, 073019.
- 1013 Krawchuk, M.B., Ruff, C.F., Yang, X., Ross, S.E., and Vazquez, A.L. (2020). Optogenetic
1014 assessment of VIP, PV, SOM and NOS inhibitory neuron activity and cerebral blood flow
1015 regulation in mouse somato-sensory cortex. *J Cereb Blood Flow Metab* 40, 1427–1440.
- 1016 Lecrux, C., and Hamel, E. (2011). The neurovascular unit in brain function and disease. *Acta*
1017 *Physiologica (Oxford, England)* 203, 47–59.
- 1018 Lee, L., Boorman, L., Glendenning, E., Christmas, C., Sharp, P., Redgrave, P., Shabir, O.,
1019 Bracci, E., Berwick, J., and Howarth, C. (2020). Key Aspects of Neurovascular Control
1020 Mediated by Specific Populations of Inhibitory Cortical Interneurons. *Cereb. Cortex* 30, 2452–
1021 2464.
- 1022 Lourenço, C.F., Ledo, A., Barbosa, R.M., and Laranjinha, J. (2017). Neurovascular-
1023 neuroenergetic coupling axis in the brain: master regulation by nitric oxide and consequences in
1024 aging and neurodegeneration. *Free Radical Biology and Medicine* 108, 668–682.
- 1025 McDowell, K.P., Berthiaume, A.-A., Tieu, T., Hartmann, D.A., and Shih, A.Y. (2021).
1026 VasoMetrics: unbiased spatiotemporal analysis of microvascular diameter in multi-photon
1027 imaging applications. *Quant Imaging Med Surg* 11, 969–982.
- 1028 Melzer, S., and Monyer, H. (2020). Diversity and function of corticopetal and corticofugal
1029 GABAergic projection neurons. *Nature Reviews Neuroscience* 21, 499–515.
- 1030 Mitchell, A.S., Czajkowski, R., Zhang, N., Jeffery, K., and Nelson, A.J.D. (2018). Retrosplenial
1031 cortex and its role in spatial cognition. *Brain Neurosci Adv* 2.
- 1032 Montagne, A., Barnes, S.R., Sweeney, M.D., Halliday, M.R., Sagare, A.P., Zhao, Z., Toga,
1033 A.W., Jacobs, R.E., Liu, C.Y., Amezcua, L., et al. (2015). Blood-brain barrier breakdown in the
1034 aging human hippocampus. *Neuron* 85, 296–302.
- 1035 Nelson, A.R., Sagare, M.A., Wang, Y., Kisler, K., Zhao, Z., and Zlokovic, B.V. (2020).
1036 Channelrhodopsin Excitation Contracts Brain Pericytes and Reduces Blood Flow in the Aging
1037 Mouse Brain in vivo. *Front Aging Neurosci* 12, 108.
- 1038 Newmaster, K.T., Nolan, Z.T., Chon, U., Vanselow, D.J., Weit, A.R., Tabbaa, M., Hidema, S.,
1039 Nishimori, K., Hammock, E.A.D., and Kim, Y. (2019). Quantitative Cellular-Resolution Map of
1040 the Oxytocin Receptor in Postnatally Developing Mouse Brains. *BioRxiv* 719229.

- 1041 Nikolakopoulou, A.M., Zhao, Z., Montagne, A., and Zlokovic, B.V. (2017). Regional early and
1042 progressive loss of brain pericytes but not vascular smooth muscle cells in adult mice with
1043 disrupted platelet-derived growth factor receptor- β signaling. *PLoS One* 12, e0176225.
- 1044 Nikolakopoulou, A.M., Montagne, A., Kisler, K., Dai, Z., Wang, Y., Huuskonen, M.T., Sagare,
1045 A.P., Lasic, D., Sweeney, M.D., Kong, P., et al. (2019). Pericyte loss leads to circulatory failure
1046 and pleiotrophin depletion causing neuron loss. *Nature Neuroscience* 22, 1089–1098.
- 1047 Packer, A.M., and Yuste, R. (2011). zhang. *J. Neurosci.* 31, 13260–13271.
- 1048 Perrenoud, Q., Geoffroy, H., Gauthier, B., Rancillac, A., Alfonsi, F., Kessarar, N., Rossier, J.,
1049 Vitalis, T., and Gallopin, T. (2012). Characterization of Type I and Type II nNOS-Expressing
1050 Interneurons in the Barrel Cortex of Mouse. *Frontiers in Neural Circuits* 6, 36.
- 1051 Pi, H.-J., Hangya, B., Kvitsiani, D., Sanders, J.I., Huang, Z.J., and Kepecs, A. (2013). Cortical
1052 interneurons that specialize in disinhibitory control. *Nature* 503, 521–524.
- 1053 Rungta, R.L., Chaigneau, E., Osmanski, B.-F., and Charpak, S. (2018). Vascular
1054 Compartmentalization of Functional Hyperemia from the Synapse to the Pia. *Neuron* 99, 362-
1055 375.e4.
- 1056 Sengillo, J.D., Winkler, E.A., Walker, C.T., Sullivan, J.S., Johnson, M., and Zlokovic, B.V.
1057 (2013). Deficiency in Mural Vascular Cells Coincides with Blood–Brain Barrier Disruption in
1058 Alzheimer’s Disease. *Brain Pathology* 23, 303–310.
- 1059 Shih, Y.-Y.I., Chen, C.-C.V., Shyu, B.-C., Lin, Z.-J., Chiang, Y.-C., Jaw, F.-S., Chen, Y.-Y., and
1060 Chang, C. (2009). A new scenario for negative functional magnetic resonance imaging signals:
1061 endogenous neurotransmission. *J Neurosci* 29, 3036–3044.
- 1062 Sohal, V.S., Zhang, F., Yizhar, O., and Deisseroth, K. (2009). Parvalbumin neurons and gamma
1063 rhythms enhance cortical circuit performance. *Nature* 459, 698–702.
- 1064 Sweeney, M.D., Ayyadurai, S., and Zlokovic, B.V. (2016). Pericytes of the neurovascular unit:
1065 key functions and signaling pathways. *Nature Neuroscience* 19, 771–783.
- 1066 Sweeney, M.D., Kisler, K., Montagne, A., Toga, A.W., and Zlokovic, B.V. (2018). The role of
1067 brain vasculature in neurodegenerative disorders. *Nature Neuroscience* 21, 1318–1331.
- 1068 Taniguchi, H., He, M., Wu, P., Kim, S., Paik, R., Sugino, K., Kvitsani, D., Fu, Y., Lu, J., Lin, Y.,
1069 et al. (2011). A Resource of Cre Driver Lines for Genetic Targeting of GABAergic Neurons in
1070 Cerebral Cortex. *Neuron* 71, 995–1013.
- 1071 Tasic, B., Yao, Z., Graybuck, L.T., Smith, K.A., Nguyen, T.N., Bertagnolli, D., Goldy, J.,
1072 Garren, E., Economo, M.N., Viswanathan, S., et al. (2018). Shared and distinct transcriptomic
1073 cell types across neocortical areas. *Nature* 563, 72–78.

- 1074 Todorov, M.I., Paetzold, J.C., Schoppe, O., Tetteh, G., Shit, S., Efremov, V., Todorov-Völgyi,
1075 K., Düring, M., Dichgans, M., Piraud, M., et al. (2020). Machine learning analysis of whole
1076 mouse brain vasculature. *Nature Methods* *17*, 442–449.
- 1077 Tomioka, R., and Rockland, K.S. (2007). Long-distance corticocortical GABAergic neurons in
1078 the adult monkey white and gray matter. *J Comp Neurol* *505*, 526–538.
- 1079 Tomioka, R., Okamoto, K., Furuta, T., Fujiyama, F., Iwasato, T., Yanagawa, Y., Obata, K.,
1080 Kaneko, T., and Tamamaki, N. (2005). Demonstration of long-range GABAergic connections
1081 distributed throughout the mouse neocortex. *Eur J Neurosci* *21*, 1587–1600.
- 1082 Tricoire, L., and Vitalis, T. (2012). Neuronal nitric oxide synthase expressing neurons: a journey
1083 from birth to neuronal circuits. *Frontiers in Neural Circuits* *6*, 82.
- 1084 Tsai, P.S., Kaufhold, J.P., Blinder, P., Friedman, B., Drew, P.J., Karten, H.J., Lyden, P.D., and
1085 Kleinfeld, D. (2009). Correlations of neuronal and microvascular densities in murine cortex
1086 revealed by direct counting and colocalization of nuclei and vessels. *The Journal of*
1087 *Neuroscience : The Official Journal of the Society for Neuroscience* *29*, 14553–14570.
- 1088 Vazquez, A.L., Fukuda, M., and Kim, S.-G. (2018). Inhibitory Neuron Activity Contributions to
1089 Hemodynamic Responses and Metabolic Load Examined Using an Inhibitory Optogenetic
1090 Mouse Model. *Cereb Cortex* *28*, 4105–4119.
- 1091 van Veluw, S.J., Hou, S.S., Calvo-Rodriguez, M., Arbel-Ornath, M., Snyder, A.C., Frosch, M.P.,
1092 Greenberg, S.M., and Bacsikai, B.J. (2020). Vasomotion as a Driving Force for Paravascular
1093 Clearance in the Awake Mouse Brain. *Neuron* *105*, 549-561.e5.
- 1094 Vergara, R.C., Jaramillo-Riveri, S., Luarte, A., Moënné-Loccoz, C., Fuentes, R., Couve, A., and
1095 Maldonado, P.E. (2019). The Energy Homeostasis Principle: Neuronal Energy Regulation Drives
1096 Local Network Dynamics Generating Behavior. *Front Comput Neurosci* *13*.
- 1097 Wang, Q., Ding, S.-L., Li, Y., Royall, J., Feng, D., Lesnar, P., Graddis, N., Naeemi, M., Facer,
1098 B., Ho, A., et al. (2020). The Allen Mouse Brain Common Coordinate Framework: A 3D
1099 Reference Atlas. *Cell* *181*, 936-953.e20.
- 1100 Williams, R.H., Vazquez-DeRose, J., Thomas, A.M., Piquet, J., Cauli, B., and Kilduff, T.S.
1101 (2017). Cortical nNOS/NK1 Receptor Neurons are Regulated by Cholinergic Projections From
1102 the Basal Forebrain. *Cerebral Cortex (New York, NY : 1991)* 1–21.
- 1103 Xiong, B., Li, A., Lou, Y., Chen, S., Long, B., Peng, J., Yang, Z., Xu, T., Yang, X., Li, X., et al.
1104 (2017). Precise Cerebral Vascular Atlas in Stereotaxic Coordinates of Whole Mouse Brain.
1105 *Frontiers in Neuroanatomy* *11*, 128.
- 1106 Zhang, Q., Roche, M., Gheres, K.W., Chaigneau, E., Kedarasetti, R.T., Haselden, W.D.,
1107 Charpak, S., and Drew, P.J. (2019a). Cerebral oxygenation during locomotion is modulated by
1108 respiration. *Nature Communications* *10*, 1–15.

- 1109 Zhang, X., Yin, X., Zhang, J., Li, A., Gong, H., Luo, Q., Zhang, H., Gao, Z., and Jiang, H.
1110 (2019b). High-resolution mapping of brain vasculature and its impairment in the hippocampus of
1111 Alzheimer’s disease mice. *Natl Sci Rev* 6, 1223–1238.
- 1112 Zhao, Z., Nelson, A.R., Betsholtz, C., and Zlokovic, B.V. (2015). Establishment and Dysfunction
1113 of the Blood-Brain Barrier. *Cell* 163, 1064–1078.
- 1114